Materials Advances

ROYAL SOCIETY OF CHEMISTRY

PAPER

View Article Online
View Journal | View Issue

Cite this: *Mater. Adv.*, 2026, 7, 986

Synthesis of a hybrid material based on a high-surface-area magnetic Fe_3O_4@TiO_2 core–shell structure and immobilized Ni–PNP aliphatic pincer complex: study of the structural, magnetic, and antibacterial properties and nonenzymatic electrochemical sensing of glucose

Fatemeh Ariaeinezhad, [a] Gholamhossein Mohammadnezhad, *[a] Oluseun Akintola [b] and Winfried Plass *[b]

Received 16th July 2025,
Accepted 24th November 2025

DOI: 10.1039/d5ma00762c

rsc.li/materials-advances

The present study reports a multistep synthesis of a hybrid material based on a Fe_3O_4@TiO_2 core–shell with an immobilized aliphatic nickel–PNP pincer complex. The Fe_3O_4@TiO_2 core–shell structure was obtained using an *in situ* method based on a controllable one-pot synthesis of TiO_2 on the surface of the Fe_3O_4 core. The hydrolysis of the molecular precursor titanium(IV) ethoxide was carried out by reaction in a mixture of ethanol, acetic acid, and water with a mole ratio of 1 : 25 : 0.1 : 4 at reflux temperature, leading to a high surface area core structure with an amorphous shell. The formation of the material and the immobilization of the complex were confirmed by FT-IR spectroscopy, XRD, FE-SEM, TEM, TGA, DSC, CHN analysis, and XPS. The amount of the immobilized nickel complex was quantified using ICP/OES analysis. The properties of the hybrid material were further investigated using UV-Vis (DRS), VSM, and argon sorption analyses. The antibacterial properties of the material were evaluated against two pathogenic strains of *Staphylococcus aureus* and *Escherichia coli* bacteria using the agar well-diffusion method. The largest inhibition effect was observed against *Staphylococcus aureus* (19 mm) by the immobilized nickel–PNP pincer complex, indicating the excellent ability of this compound to be utilized as an antibacterial agent against pathogenic strains. Furthermore, the immobilized aliphatic nickel–PNP pincer complex was used as a modified electrode for nonenzymatic glucose sensing using cyclic voltammetry (CV) and differential pulse voltammetry (DPV) methods. The modified electrode with Nafion exhibited linear ranges of 5 μM–0.1 mM and 0.1–7 mM with high sensitivities of 3692 and 276 μA $mM^{-1}.cm^{-2}$, respectively, with a low detection limit of 0.894 μM (S/N = 3) in an alkaline medium for glucose determination. The results from the nonenzymatic glucose detection experiments demonstrate that the Fe_3O_4@TiO_2-PTES@NiPNP/GCE is a suitable candidate for glucose quantification.

Introduction

The development of pincer metal complexes, due to their robust architectures, has played a significant role in the improvement of chemical processes over the past century and has contributed significantly to global progress in medicine,[1,2] gas sensors,[3,4] switching,[5,6] and catalysis.[7,8] Pincer ligands are generally described as *mer*-tridentate ligands bound to the metal center through three donor atoms in the main backbones and form two-, five- or six-membered rings.[9] In the past few decades, most investigations have focused on the design and synthesis of pincer complexes as effective homogeneous catalysts for chemical and biological reactions, even under harsh conditions. Despite the success of homogeneous catalysts, due to their high activity and selectivity in many processes, they face challenges such as catalyst separation and recycling, as well as the use of costly methods for the purification of the products.[9,10] However, heterogeneous catalysts have significant advantages, such as ease of catalyst separation from the reaction mixture and high recyclability, but they have poor catalytic selectivity.[9–11] The immobilization of an active complex as a homogenous catalyst onto solid supports to produce

[a] *Department of Chemistry, Isfahan University of Technology, Isfahan, 84156-83111, Islamic Republic of Iran. E-mail: mohammadnezhad@iut.ac.ir*
[b] *Institut für Anorganische und Analytische Chemie, Friedrich-Schiller-Universität Jena, Humboldtstr. 8, 07743 Jena, Germany. E-mail: sekr.plass@uni-jena.de*

hybrid catalyst systems is an interesting strategy that is both selective and recyclable.[9,10] Therefore, the choice of a suitable solid support plays an important role in the immobilization method and performance for different purposes. Thus far, various pincer ligands have been immobilized onto different types of organic and inorganic solid supports, such as mesoporous silica, titania, magnetic nanoparticles, metal–organic frameworks (MOFs), polymers, and dendrimers.[9,12–17] Among various supports, titania, due to its low cost, high surface area, excellent chemical stability, non-toxicity, antimicrobial, and high photocatalytic activity,[18–21] and magnetic nanoparticles, due to their ease of separation,[22] have attracted much attention in the development of hybrid catalyst systems.[9,14] Therefore, the core–shell structures obtained by combining TiO_2 nanoparticles and magnetic nanomaterials of Fe_3O_4 not only possess the advantages of efficient catalyst recovery and desirable specific surface area but can also be a promising method for decreasing the rate of electron/hole recombination and improving their photocatalytic performance.[19,22] The immobilization of pincer/metal complexes on solid supports provides recoverability and reusability. Another unique advantage of the immobilization of the pincer complex is the low leaching of metal due to the strong ligation of the pincer ligand, which results in improved catalytic performance.[23] However, the immobilization of aliphatic pincer complexes based on phosphorus ligands onto solid supports has rarely been reported. Liang *et al.* reported the immobilization of the PNP pincer ligand bis[2-diphenylphosphinoethyl]amine *via* covalent attachment on a nanodiamond support. In this immobilization method, the surface carboxyl groups selectively reacted with the amino groups of the PNP ligands to form the PNP-ND sample. Subsequently, the Rh species were coordinated with the surface PNP ligand after adding an organic solution of the Rh precursor to the PNP-ND and then were reduced under a hydrogen atmosphere at 120 °C for 2 h. Additionally, the catalytic results showed that the immobilized pincer complex had catalytic performance similar to that of its homogeneous counterparts in styrene hydroformylation.[8]

Over the past decade, studies have shown that waterborne diseases caused by pathogens, like *E. coli* and *Enterobacter aerogenes*, account for 80% of reported diseases and up to 40–80% of infant mortality worldwide.[24] Traditional water disinfection methods, including advanced oxidation processes, UV radiation,[24,25] ozonation,[24,26,27] membrane bioreactors,[24,28] and chlorination,[24,29] are costly and generate harmful by-products.[24,29] Chlorination, though widely used, is ineffective against resistant bacteria and generates carcinogenic compounds.[24,30] Therefore, to develop safer, more efficient disinfection and environmentally friendly strategies, researchers have explored nanomaterials and pincer complexes with antibacterial properties.[24,31–34] Among the nanoparticles, TiO_2 exhibits strong antimicrobial effects without aggressive oxidation against both Gram-positive and Gram-negative bacteria. Surface modifications further enhance their antibacterial efficiency.[24,35] Additionally, metal complexes exhibit significant antimicrobial activity. The reported mechanism involves an increase in the lipophilicity of metal complexes, making it easier for them to penetrate the cell membranes of microorganisms.[31–33]

Glucose is a vital carbohydrate that plays an essential role in the human body.[36] It is closely linked to numerous physiological processes and is important in areas such as human health and medical applications.[37] Moreover, the accurate measurement of glucose levels has been widely studied across various disciplines, such as biotechnology, clinical diagnostics, and the food industry.[38,39] Due to considerable variations in glucose concentrations across different biological samples (such as sweat and saliva), there is a need for highly sensitive nonenzymatic and enzymatic sensors to ensure precise detection. To address this need, researchers have developed a range of electrochemical sensors utilizing nanomaterials.[40,41] Among these, nanomaterials based on nickel have garnered particular attention due to their exclusive redox behavior (Ni^{II}/Ni^{III}), high surface-to-electroactive area, and biocompatibility.[42] Despite numerous studies on different nickel-based nanomaterials, the electrocatalytic behavior of immobilized aliphatic nickel–PNP pincer complexes in glucose oxidation has not yet been explored.

In our previously published article, the nickel complex [NiCl(P^N^P)]Cl·EtOH was prepared based on a P^N^P type pincer ligand (P^N^P = bis[(2-diphenylphosphine)ethyl]amine), and its electrocatalytic and anticancer activities were studied. The results have shown that the pincer nickel complex is an efficient electrocatalyst for hydrogen evolution at the potential of the Ni(II/I) couple, and the anticancer effect of this complex depends on time and concentration.[2] In this work, we report a controllable one-pot synthesis (hydrolysis) and an *in situ* method to prepare Fe_3O_4@TiO_2 core–shell using titanium ethoxide as a single-source molecular precursor. Then, the immobilization of a nickel complex prepared based on a P^N^P type pincer ligand on Fe_3O_4@amorphousTiO_2 core–shell as a support *via* anchored attachments is described. The antimicrobial properties of magnetite nanoparticles, amorphous TiO_2, the immobilized nickel(II) complex, and Fe_3O_4@amorphous TiO_2 core–shell were investigated by applying the agar well-diffusion method. Additionally, for the first time, the electrocatalytic properties of the immobilized aliphatic nickel–PNP pincer complex toward glucose oxidation were studied.

Experimental section

Materials and methods

Bis(diphenylphosphinethyl)amine hydrochloride (P^N^P·HCl, the pincer ligand) and [Ni(P^N^P)Cl]Cl·EtOH were prepared according to our previously published article and were characterized by ^1H and ^{13}C NMR.[2] Ferric chloride hexahydrate ($FeCl_3·6H_2O$, Daejung, 97%), ferrous chloride tetrahydrate ($FeCl_2·4H_2O$, Daejung, 98%), aqueous ammonia (NH_3 (aq), Dr Mojallali, 25%), titanium(IV) ethoxide ($C_8H_{20}O_4Ti$, Merck, >95%), glacial acetic acid ($C_2H_4O_2$, Ameretat Shimi, 99.5–100.5%), (3-chloropropyl)triethoxysilane (CPTES, $C_9H_{21}ClO_3Si$, Merck, 95%), triethylamine ($C_6H_{15}N$, Merck, 95%), D-glucose

($C_6H_{12}O_6$, Merck) and sodium hydroxide (NaOH, Merck, >97%) were used without further purification. Toluene ($C_6H_5CH_3$, Dr Mojallali, 98%) was dried under reflux with sodium and benzophenone, as an indicator, before use. Additionally, ethanol (C_2H_5OH, Bidestan, 99.5%) was dried over sodium and distilled before use. All experiments were carried out using standard Schlenk techniques under an argon atmosphere. All samples, including the aqueous solutions, were prepared with deionized water.

Fourier-transform infrared (FT-IR) spectra were recorded using Tensor 27 (Bruker, Germany) at room temperature in the wavelength range of 400–4500 cm^{-1}. Routine powder X-ray diffraction (PXRD) patterns to investigate the effect of the immobilization process on the crystallinity and phase composition of the support material were collected using a Rigaku MiniFlex diffractometer with a Cu Kα tube (λ = 1.541 Å) in the 2θ range of 10°–80°. Thermogravimetric analyses (TGAs) of the samples were carried out under an air atmosphere using a Netzsch STA 449F1 instrument (Germany) from room temperature to 800 °C at a heating rate of 10 K min^{-1}. Elemental analyses (EA, C, H, and N) were performed using Leco CHNS-932 or an El Vario III elemental analyzer (Germany). Inductively coupled plasma optical emission spectrometry (ICP-OES) was performed using an Optima 7300 DV (PerkinElmer, American) spectrometer. The UV-Vis diffuse reflectance spectra of the solid samples (UV-Vis DRS) were recorded in the wavelength range of 200–800 nm using a Shimadzu 2450 spectrophotometer equipped with a diffuse reflectance unit and subsequently transformed into the absorbance coefficient using the Kubelka–Munk function. Field emission scanning electron microscopy (FE-SEM) with energy dispersive X-ray spectroscopy (EDS) and transmission electron microscopy (TEM) images were obtained using Quanta 450 FEG (FEI, USA) and Philips CM 120 (Netherlands) devices, respectively. Argon adsorption–desorption isotherms were recorded using an Autosorb-IQ instrument from Quantachrome Instruments Corporation at 87 K with the aid of a CryoSync accessory. Pore size distribution curves were calculated by fitting the experimental data using a non-local density functional theory (NLDFT) kernel based on adsorption models for Ar on zeolites/silica at 87 K with cylindrical pores, which was provided by QUANTACHROME Instruments.[43] The Brunauer–Emmett–Teller (BET) surface areas for both materials were determined from the adsorption data over different relative pressure ranges, all between 0.025 and 0.28, while ensuring compliance with the consistency criteria (Table S1).[44] The magnetization of the samples was measured using a vibrating sample magnetometer with an applied magnetic field of ±10 kOe at room temperature (VSM, Meghnatis Daghigh Kavir Co., Kashan, Iran). X-Ray photoelectron spectra (XPS) were recorded using a Bes Tec (EA10, Germany) system with Al Kα X-ray as the excitation source at 1486.6 eV. The binding energy was calibrated for the C 1s signal at 284.8 eV. All electrochemical experiments were performed using a SAMA500 electro-analyzer system (Iran) and driven by SAMA software at room temperature. A conventional three-electrode system was used, with a modified glassy carbon electrode (2 mm in diameter) as the working electrode, platinum 99.99% (0.5 mm in diameter and 5 mm in length with spherical tip) as the counter electrode, and saturated Ag/AgCl as the reference electrode. During the three-electrode experiments, charge flow (current density) primarily occurs between the working and counter electrodes, while the potential of the working electrode is measured based on the reference electrode.

Preparation of the magnetic Fe_3O_4@TiO_2 core–shell nanocomposite

Fe_3O_4 nanoparticles, as magnetic cores, were prepared using a facile co-precipitation method reported previously.[45] The Fe_3O_4@TiO_2 core–shell nanocomposites were obtained using an *in situ* method of hydrolysis of titanium(IV) ethoxide according to the following process. First, as-prepared Fe_3O_4 nanoparticles (1.00 g) were dispersed through ultrasonic treatment in anhydrous ethanol (35 mL) for 20 min under an Ar atmosphere. Then, titanium(IV) ethoxide (5 mL) was added dropwise into the above suspension under an Ar atmosphere and stirred mechanically for 0.5 h. Subsequently, to achieve controlled hydrolysis, a solution of deionized water (1.73 mL) and acetic acid (0.14 mL) was added dropwise into the mixture at 78 °C under vigorous stirring. The reaction mixture was stirred under reflux overnight. Finally, the brown precipitate was magnetically separated and dried under vacuum at 50 °C for 3 h.

Preparation of chloro-functionalized magnetic Fe_3O_4@TiO_2 core–shell nanocomposite (Fe_3O_4@TiO_2-CPTES)

The surface modification of Fe_3O_4@TiO_2 core–shell nanocomposites was performed using (3-chloropropyl)triethoxysilane (CPTES), as described below. Briefly, the as-prepared magnetic core–shell Fe_3O_4@TiO_2 (1.2 g) was added to dry toluene (15 mL) and sonicated for 20 min at room temperature under an argon atmosphere. Then, CPTES (3 mL) was added, and the mixture was refluxed for 24 h under an argon atmosphere to produce Fe_3O_4@TiO_2-CPTES. Next, the as-prepared precipitate was collected using a supermagnet and dried under vacuum at 50 °C for 3 h.

Preparation of the immobilized Ni–PNP aliphatic pincer complex on Fe_3O_4@TiO_2-CPTES (Fe_3O_4@TiO_2-PTES@NiPNP)

[Ni(P^N^P)Cl]Cl pincer complex was synthesized according to a method reported in our previous study.[2] Then, the Fe_3O_4@TiO_2-CPTES support (0.2 g) was dispersed in dry ethanol (7 mL) by sonication for 30 min under an argon atmosphere. Subsequently, triethylamine (0.5 mL) and [Ni(P^N^P)Cl]Cl (0.1 g in 5 mL anhydrous ethanol) were added dropwise to the reaction mixture and were refluxed for 12 h under an argon atmosphere. The mixture was cooled to room temperature, and the product was magnetically separated and washed three times with ethanol. The resulting brown powder was dried under a vacuum at 50 °C for 3 h and used for analysis and reactions.

Antibacterial assay using the well diffusion method

The antibacterial activities of Fe_3O_4, Fe_3O_4@TiO_2, Fe_3O_4@TiO_2-CPTES, and Fe_3O_4@TiO_2-PTES@NiPNP were determined using

the well diffusion method against two species of bacteria: Gram-negative *Escherichia coli* (ATCC 25922) and Gram-positive *Staphylococcus aureus* (ATCC 25923). These were model bacteria purchased from the Persian type culture collection. In this study, 10 μL of the bacterial suspension with an optical density equivalent to 0.5 MacFarland standards, corresponding to a bacterial concentration of 1.5×10^8 CFU mL^{-1}, were spread on the surface of each sterilized Petri agar plate. The wells were then created in the plates using a sterile cork-borer, and 40 mg of the as-prepared nanostructures were transferred into each well. In addition, a sterile disk containing 10 μg of standard gentamicin was used as a positive control and placed in each Petri dish at an appropriate distance from the wells to ensure an accurate comparison and avoid cross-contamination. Finally, the agar culture mediums were incubated overnight at 37 °C. After 24 hours, zones of growth inhibition were observed, and their diameters (in mm) were measured and compared with those of the control.

Preparation of a modified electrode for sensing glucose

Prior to the surface modification, the glassy carbon electrode was abraded with emery paper to obtain a mirror-like surface, and the washing treatment was performed with deionized water in a sonication bath for 1–2 min. In order to prepare the GC electrode modified with TiO_2, Fe_3O_4@TiO_2, and Fe_3O_4@TiO_2-PTES@NiPNP, first, 3 mg of each sample was dispersed in 1 mL of absolute ethanol and then sonicated for 10 min so that a homogeneous suspension was formed. Then, 5 μL of each suspension was pipetted onto the cleaned GCE surface, and 1 μL of a 2% Nafion solution was drop-cast on the modified electrode surface and dried at room temperature (25 °C). The prepared Fe_3O_4@TiO_2-PTES@NiPNP/GCE-modified electrode was used as a working electrode in all electrochemical measurements.

Results and discussions

Fe_3O_4@TiO_2 core–shell nanostructures and the immobilization of the nickel–PNP pincer complex

As shown in Scheme 1, the [Ni(P^N^P)Cl]Cl pincer complex was covalently attached to the modified magnetic Fe_3O_4@TiO_2 support. To achieve this, a three-step synthesis procedure was employed in which the pincer complex and magnetite nanoparticles were prepared according to previous reports.[2,45] In the first step, an amorphous TiO_2 shell with a high surface area was coated on a monodisperse, ethanol-dispersible magnetic core by the controlled hydrolysis of titanium(IV) ethoxide using a simple and surfactant-free method (*in situ* method) in a short time. To obtain a uniform shell, the hydrolysis rate of titanium(IV) ethoxide must be controlled. This was done by the addition of an acetic acid/water solution to a solution of titanium ethoxide in its parent alcohol (ethanol) at reflux temperatures, where the molar ratio between the reaction components, alkoxide : ethanol : acid : water, was 1 : 25 : 0.1 : 4.[20] In the second step, the reactive (3-chloropropyl)triethoxysilane (CPTES) was covalently attached

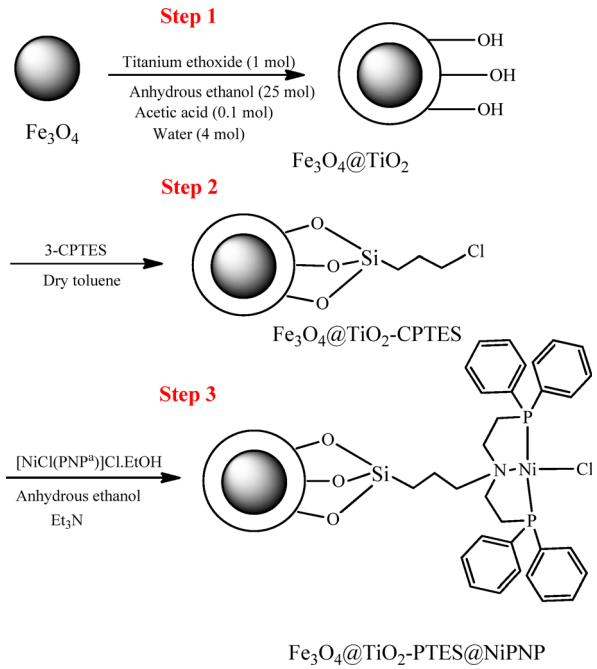

Scheme 1 Preparation of the Fe_3O_4@TiO_2 core–shell nanostructure and the immobilization of the nickel–PNP pincer complex.

to the modified magnetic support (Fe_3O_4@TiO_2) as a linker, resulting in a chloro-functionalized magnetic support (Fe_3O_4@TiO_2-CPTES). In the third step, the chlorine groups on the surface of Fe_3O_4@TiO_2-CPTES were reacted with amine groups of the P^N^P pincer complex in the presence of an excess amount of triethylamine as a base. Finally, for the first time, the nickel–PNP pincer complex was immobilized on the surface of Fe_3O_4@TiO_2 core–shell under reflux conditions in the presence of triethylamine as a base.

Fourier-transform infrared spectroscopy (FT-IR)

Fig. 1 shows the FT-IR spectra of Fe_3O_4, Fe_3O_4@TiO_2, Fe_3O_4@TiO_2-CPTES, and Fe_3O_4@TiO_2-PTES@NiPNP in the range of 400–4000 cm^{-1}. The weak absorption band at around 1630 cm^{-1} and the broad absorption band at around 3400 cm^{-1} present in all samples correspond to the bending and stretching vibrations of the hydroxyl groups or adsorbed water on the surface of the samples.[20,46,47] After coating the Fe_3O_4 surface with a TiO_2 shell to form Fe_3O_4@TiO_2 *via* the hydrolysis–condensation processes, absorption bands are observed at 1539 and 1442 cm^{-1}, corresponding to the asymmetric and symmetric stretching vibrations of the metal carboxylate, respectively.[20,47–49] As reported in our previous study, the distance between these two peaks reflects the nature of the interaction between carboxyl groups and titanium. Here, the distance is about 95 cm^{-1}, conforming to the formation of a chelating bidentate ligand, which leads to the formation of small and well-dispersed particles in the early stages of the reaction.[20,48,50] Additionally, the absorption peaks at 2854 and 2968 cm^{-1} correspond to the aliphatic stretching vibrations of CH_2, and the absorption peaks at 1031 and 1124 cm^{-1} represent C–O stretching vibrations due

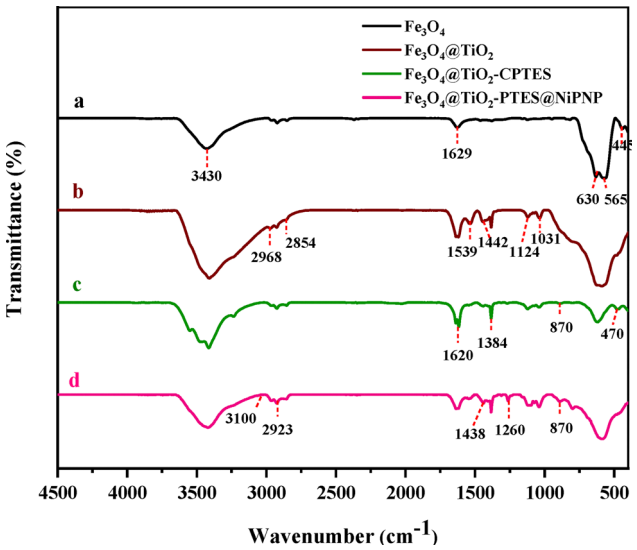

Fig. 1 FT-IR spectra of (a) Fe_3O_4, (b) Fe_3O_4@TiO_2, (c) Fe_3O_4@TiO_2-CPTES nanostructures, and (d) the immobilized nickel–PNP pincer complex, Fe_3O_4@TiO_2-PTES@NiPNP.

to ester formation from the reaction of acetic acid with ethanol.[20,48,49,51] Fe_3O_4@TiO_2 spectrum shows an absorption peak at around 400–700 cm^{-1}, attributed to the stretching vibration of O–Ti–O and Ti–O, and was relatively broader due to overlapping with the Fe–O peak compared with the Fe_3O_4 spectrum.[20,52–54] Due to the influence of the TiO_2 shell, the characteristic band intensities of Fe_3O_4 at 445, 630, and 565 cm^{-1} became broader.[52–54] Additionally, the intensity of the band associated with hydroxyl groups on Fe_3O_4@TiO_2 is higher than that on Fe_3O_4. The results could be an indication of TiO_2 formation on the surface of the Fe_3O_4 and the successful preparation of Fe_3O_4@TiO_2.[52] After the modification of the surface of the magnetic Fe_3O_4@TiO_2 with CPTES groups, the band intensities increased at around 3400 cm^{-1}, 1622 cm^{-1}, and 2858–2962 cm^{-1}, which are related to O–H vibration mode from Si–OH, twisting vibration mode of adsorbed water HO–H and the C–H stretching vibrations of the anchoring propyl groups, respectively.[55–57] The absorption bands located in the regions of 470, 870 cm^{-1}, and 1000–1100 cm^{-1} were assigned to the bending vibrations of the Si–O–Si band and the stretching vibrations of the Si–O band.[55,58] The absorption band at 570 cm^{-1} was attributed to the Si–O–Ti, which overlapped with the Ti–O vibration.[56,58] However, the stretching vibration of unreacted C–Cl bands and the stretching vibration of Si–C bands cannot be detected in this spectrum because their bands are completely covered by the strong peaks of Si–O–Si and Ti–O–Ti bonds.[14,56,59] In the spectrum of the immobilized nickel–PNP pincer complex, the absorption bands are related to CH at around 3100 cm^{-1} and C=C of the aromatic rings of diphenylphosphine at around 1400 and 1600 cm^{-1}. The absorption bands related to the stretching and bending vibrations of aliphatic CH and CH_2 of bis(ethylamine) moieties at around 2923 and 1438 cm^{-1} overlap with the peaks in other samples, respectively.[2] A new band appears at around 1260 cm^{-1} and can be assigned to the C–N stretching vibrations of the pincer ligand and the newly formed band by the immobilization process.

Powder X-ray diffraction (PXRD) pattern

Powder X-ray diffraction (PXRD) patterns were used to investigate the effect of the immobilization process on the crystallinity and phase composition of the support materials. Fig. 2(a) illustrates the powder diffractograms of the Fe_3O_4 nanoparticles by a series of diffraction peaks at around $2\theta = 18.52^\circ$, 30.1°, 35.45°, 37.14°, 43.08°, 53.45°, 56.98°, 62.57°, 70.99°, 74.02°, and 76.64°, which correspond to the (020), (220), (311), (222), (400), (422), (511), (440), (533), (444), and (642) planes of the cubic Fe_3O_4 crystal structure, respectively (JCPDS CAS no. 00-019-0629).[45] After the coating of magnetite with TiO_2 nanostructures by the hydrolysis process to form a core–shell structure, no additional diffraction peaks were detected, indicating the amorphous phase of TiO_2 (Fig. 2(b)). Additionally, no difference was observed between the powder diffractograms for other materials before and after grafting of the nickel–PNP pincer complex on Fe_3O_4@TiO_2-CPTES, indicating that the immobilization process neither changed the phase composition nor the crystalline structure (Fig. 2(c) and (d)). However, the reflexes related to magnetite decreased after each step, indicating that the modification processes were successful. The average sizes of the Fe_3O_4 nanoparticles before and after the TiO_2 coating and immobilization of the nickel complex were calculated from the full width at half maximum (FWHM) of the major peaks by Debye–Scherer's equation (eqn (1)):

$$D = \frac{K\lambda}{\beta \cos\theta} \quad (1)$$

where D is the average size, k is the Debye–Scherrer constant taken as 0.9, λ is the wavelength of X-ray radiation (Cu Kα, $\lambda = 1.5406$ Å), β is the FWHM of the diffraction line, and θ is the diffraction angle.[20] The average crystallite sizes of the Fe_3O_4, Fe_3O_4@TiO_2, Fe_3O_4@TiO_2-CPTES, and Fe_3O_4@TiO_2-PTES@NiPNP samples

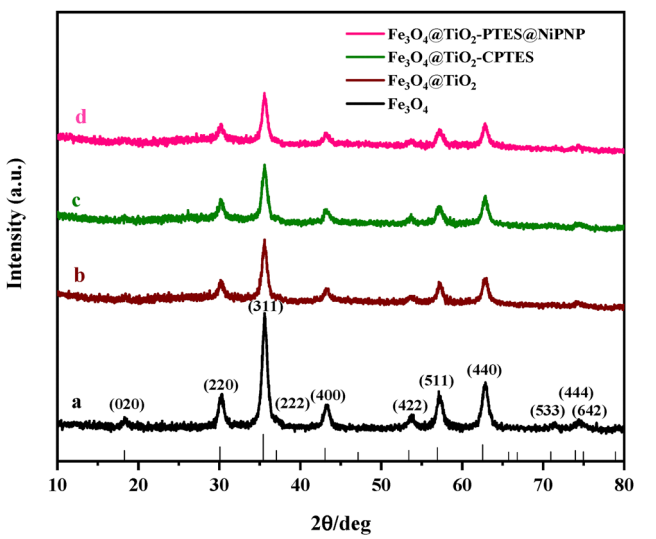

Fig. 2 PXRD patterns of (a) Fe_3O_4, (b) Fe_3O_4@TiO_2, (c) Fe_3O_4@TiO_2-CPTES, and (d) the immobilized nickel–PNP pincer complex.

were determined from the (311) diffraction peak, as the major peak with the highest intensity, and were calculated as 10.6, 8.2, 7.6, and 7.6 nm, respectively. This decrease in crystallite size was also observed previously and could be attributed to the deagglomeration of Fe_3O_4 upon coating, surface reconstruction, lattice contraction, and macro-strain enhancement by the surface modification process.[60]

UV-visible diffuse reflectance spectroscopy (UV-Vis DRS)

The optical properties of Fe_3O_4, Fe_3O_4@TiO_2, Fe_3O_4@TiO_2-CPTES, and Fe_3O_4@TiO_2-PTES@NiPNP were investigated using UV-visible diffuse reflectance spectroscopy (DRS). The results are depicted in Fig. 3(a). The magnetic Fe_3O_4 nanoparticles exhibited broad absorption bands in both ultraviolet and visible light regions.[61] However, for pure as-prepared TiO_2 nanostructure, according to our previous work, the absorption is limited to the ultraviolet light region.[20] The Fe_3O_4@TiO_2, Fe_3O_4@TiO_2-CPTES, and Fe_3O_4@TiO_2-PTES@NiPNP nanostructures display three specific high-energy bands in the UV region at around 210–320 nm. These bands are assigned to the π–π* and n → π* transitions, which can be interpreted as intra-ligand electronic charge transfer in the complex and Fe_3O_4@TiO_2 support.[14] Moreover, the ligand-metal charge transfers of O^{2-} 2p → Fe^{3+}(Ti^{4+}) 3d occur with the absorption of light in the UV region.[14,62,63] The absorption edge in the Fe_3O_4@TiO_2 support shows a red shift close to the visible region (around 350 nm), and the absorption intensity increases compared to the as-synthesized TiO_2 nanomaterials in our previous research (used to be at ~330 nm).[20] This can be attributed to iron ion insertion into the structure of titanium dioxide, which creates an intermediate layer of energy between the valence and conduction bands in titanium dioxide, resulting in a decrease in the band gap of TiO_2 and shifting the absorption towards the visible region.[62] The appearance of two new peaks in the Fe_3O_4@TiO_2 sample, before and after the immobilization of the nickel–PNP pincer complex at around 400 and 500 nm regions, can be assigned to the inter-ligand charge transition and the d → d transitions in metal centers (iron and nickel), respectively.[14,64]

Moreover, absorption intensity after the immobilization of the nickel–PNP pincer complex was enhanced in comparison with the magnetic Fe_3O_4@TiO_2 support at around a wavelength of 350–800 nm. This result indicates that the immobilization of the nickel–PNP pincer complex can promote the absorption of visible light. The band gap of these samples was calculated using the Tauc plot $(F(R)h\nu)^{1/2}$ *vs.* $h\nu$, assuming that the Fe_3O_4@TiO_2 sample after the immobilization of the nickel–PNP pincer complex is a semiconductor with an indirect band gap (Fig. 3(b)). It can be observed that the band gaps of Fe_3O_4, Fe_3O_4@TiO_2, Fe_3O_4@TiO_2-CPTES, and Fe_3O_4@TiO_2-PTES@NiPNP are 1.65, 2.42, 2.36, and 2.16 eV, respectively, which are lower than that of TiO_2 (3.2 eV),[20] indicating the high potential of samples for visible light absorption. The decrease in the band gap compared to TiO_2 could be due to providing new energy levels below the conduction band after the immobilization of the nickel–PNP pincer complex or the presence of iron and oxygen vacancies in the Fe_3O_4@TiO_2 structure.[14]

Thermogravimetric and elemental analyses (TGA, CHN, and ICP-OES)

Fig. 4 shows the thermal analysis curves of the as-prepared samples in the immobilization process of the nickel–PNP pincer complex on Fe_3O_4@TiO_2. The weight loss observed for all samples from room temperature to below 200 °C (Fe_3O_4@TiO_2: 12.6 wt%, Fe_3O_4@TiO_2-CPTES: 9.0 wt%, and Fe_3O_4@TiO_2-PTES@NiPNP: 4.7 wt%) is attributed to the removal of physically adsorbed water or solvent molecules.[14,20] The weight loss observed at about 200–550 °C (Fe_3O_4@TiO_2: 10.7 wt%, Fe_3O_4@TiO_2-CPTES: 13.0 wt%, and Fe_3O_4@TiO_2-PTES@NiPNP: 12.5 wt%) can be attributed to the thermal degradation of the organic groups. Additionally, three exothermic peaks were observed in the DSC curves of these samples at around 260, 360, and 420 °C, which are

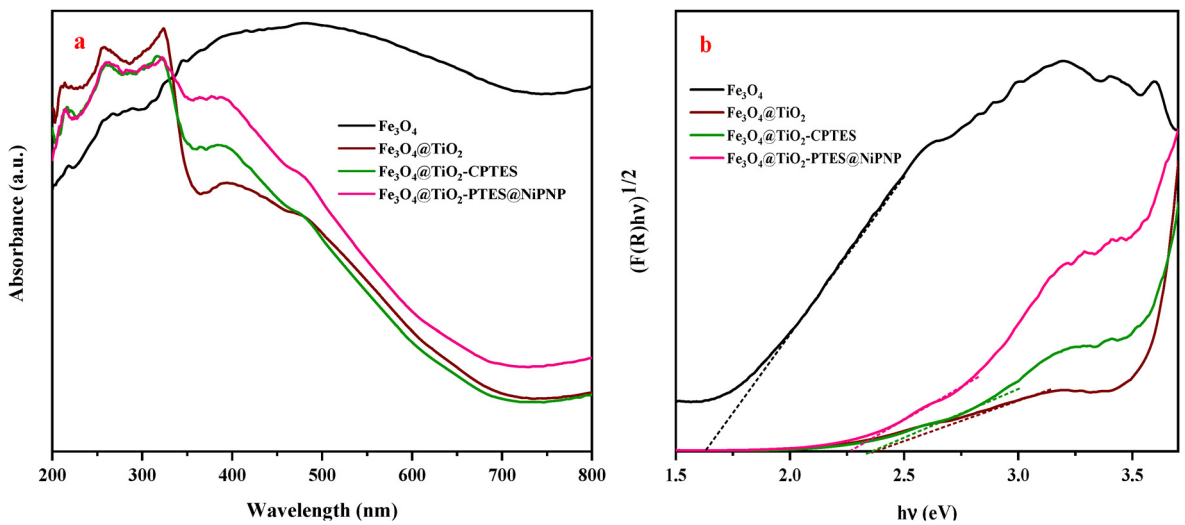

Fig. 3 (a) UV-vis DRS spectra and (b) Tauc plots of Fe_3O_4, Fe_3O_4@TiO_2, Fe_3O_4@TiO_2-CPTES, and Fe_3O_4@TiO_2-PTES@NiPNP.

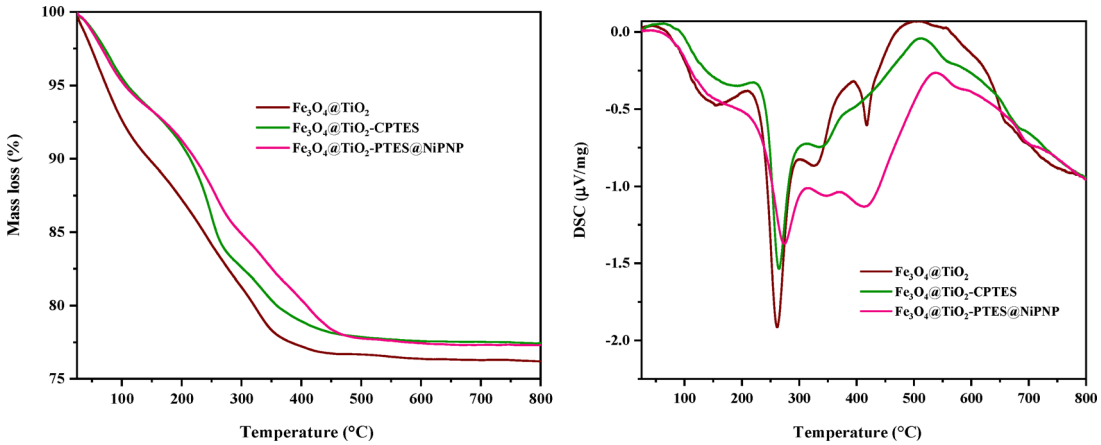

Fig. 4 (a) Thermogravimetric and (b) differential scanning calorimetry curves of Fe_3O_4, Fe_3O_4@TiO_2, Fe_3O_4@TiO_2-CPTES, and Fe_3O_4@TiO_2-PTES@NiPNP.

consistent with the weight losses associated with the removal of organic compounds (including unhydrolyzed ethoxo groups, residual acetate ligands, chloropropyl groups, and PNP pincer ligands) and the phase change in the TiO_2 from amorphous to anatase.[14,20] The low weight loss of up to 550 °C for all samples can be attributed to the further combustion of carbonaceous species and the high thermal stability of the samples.[14] In addition to TGA, elemental analysis (EA) was also used to calculate the percentage of immobilized organic compounds onto Fe_3O_4@TiO_2. CHN analysis showed that after the reaction of CPTES with Fe_3O_4@TiO_2 and then with the nickel–PNP pincer complex, the weight percent of carbon and nitrogen increased, demonstrating the successful attachment of the nickel–PNP pincer complex to Fe_3O_4@TiO_2-CPTES. In this regard, weight losses were also calculated based on the results of EA (C, N, and H values) and the amount of Cl based on the theoretical Cl/N ratio (see Table 1). The weight losses determined from elemental analyses and TGA measurements for the individual immobilization steps on Fe_3O_4@TiO_2 are in good agreement (Table 1, columns 5 and 6). According to this calculation, it can be assessed that the loading amount of chloropropyl groups and the nickel–PNP pincer complex on the surface of Fe_3O_4@TiO_2 are around 0.82 and 0.22 mmol g^{-1}, respectively. The amount of nickel present in the immobilized nickel–PNP pincer complex after the final immobilization step was determined by inductively coupled plasma optical emission spectrometry (ICP-OES) analysis. The results showed that this sample contained 0.14 mmol g^{-1} of nickel; in fact, about 60% of the nickel–PNP complex was immobilized on the surface of Fe_3O_4@TiO_2.

Field emission scanning and transmission electron microscopies (FE-SEM and TEM)

The surface characteristics, morphology, and size distribution of the nanostructures prepared in each step were monitored by field emission scanning electron microscopy, energy dispersive X-ray spectroscopy and transmission electron microscopy (FE-SEM, EDS, and TEM). As can be observed in Fig. 5(a)–(d), SEM images of all the materials consist of interconnected quasi-spherical nanostructures, indicating that the initial quasi-spherical morphology of Fe_3O_4 was preserved. Additionally, the surface of the samples was much rougher than that of Fe_3O_4, which showed that the TiO_2 nanostructure was coated on the surface of Fe_3O_4, and the nickel–PNP pincer complex was immobilized onto the surface of Fe_3O_4@TiO_2. Moreover, the energy-dispersive X-ray spectroscopy (EDS) analysis (Fig. 6) of Fe_3O_4@TiO_2-PTES@NiPNP reveals the existence of elements such as Fe, Ti, Ni, C, Cl, N, P, and O, which confirms the

Table 1 Results for elemental analysis (EA) and experimental TGA- and EA-based weight loss with the calculated values for loading amounts of organic compounds after functionalizing Fe_3O_4@TiO_2 and immobilization of the nickel–PNP pincer complex

Sample	C (%)	H (%)	N (%)	TGA weight loss[a] (%)	EA weight loss[b] (%)	Theoretical weight loss[c] (%)	Overall yield[d] (%)	Grafting (mmol g^{-1})
Fe_3O_4@TiO_2	7.57	2.07	—	10.72	9.64	—	—	—
Fe_3O_4@TiO_2-CPTES	10.53	2.47	—	13.25	15.92	14.73	100	0.82[e]
Fe_3O_4@TiO_2-PTES@NiPNP	11.49	2.48	0.31	14.28	15.65	20.51	73	0.22[f]

[a] Weight loss between 200 and 550 °C is related to the immobilized organic groups. [b] Summation of the experimental amounts of C, H, and N, and the calculated amounts of Cl and P. The amounts of Cl and P are calculated based on the theoretical Cl : C and P : N ratios; the amount of C is derived from the difference in the weight percentages of C before and after modification. [c] The values were calculated based on the following formula: theoretical weight loss (%) = (mass of the initial organic content + mass of the added organic content)/(100 + mass of the added part) × 100. Notably, for Fe_3O_4@TiO_2-PTES@NiPNP, the Cl values should be deduced from the "mass of the initial organic content." [d] The coverage achieved with (3-chloropropyl)triethoxysilane (CPTES) is set as 100%. The other value was calculated based on the average experimental weight loss (TGA and EA) relative to the theoretical weight loss. [e] The amount of chloropropyl group loading is calculated based on the difference in the carbon content from CHN analysis. [f] The amount of complex loading is calculated based on the nitrogen content from the CHN analysis.

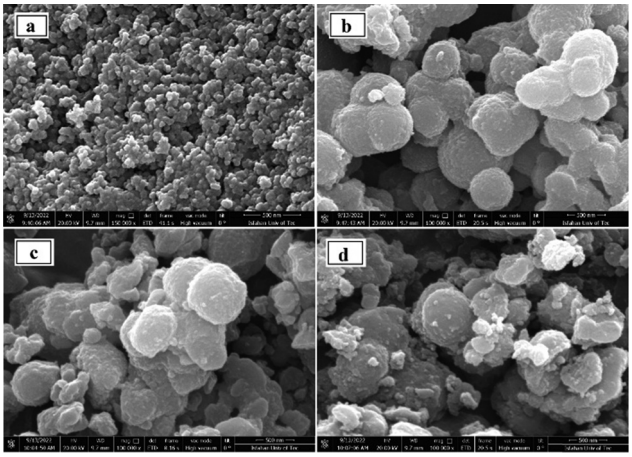

Fig. 5 FE-SEM images of (a) Fe_3O_4, (b) Fe_3O_4@TiO_2, (c) Fe_3O_4@TiO_2-CPTES, and Fe_3O_4@TiO_2-PTES@NiPNP.

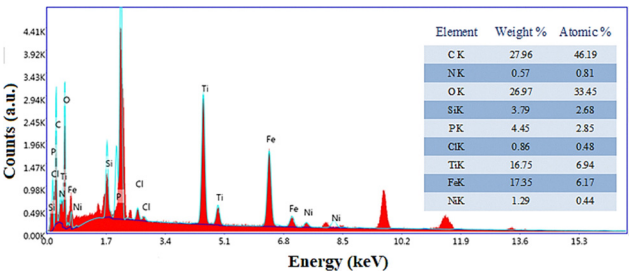

Fig. 6 EDS patterns of Fe_3O_4@TiO_2-PTES@NiPNP; the immobilized nickel–PNP pincer complex onto the surface of the Fe_3O_4@TiO_2 core–shell.

formation of Fe_3O_4@TiO_2 and the immobilization of nickel–PNP pincer complex on the surface of the Fe_3O_4@TiO_2 nanostructures. The EDS mapping of this sample (Fig. 7) shows the homogeneous distribution of all these elements. The distribution of Ti and Fe is denser than that of the other elements, which is due to the higher content of TiO_2 and Fe_3O_4, respectively. In addition, the presence of red (N) and light-gray (Ni) dots proved that the nickel–PNP pincer complex was successfully immobilized onto the surface of Fe_3O_4@TiO_2. The corresponding TEM images depicted in Fig. 8(a)–(d) confirm the quasi-spherical morphology of the Fe_3O_4 and the core–shell Fe_3O_4@TiO_2 nanostructures. As shown in Fig. 8(b) and (c), these Fe_3O_4 cores are covered by approximately 13 nm amorphous TiO_2 layers. The lattice fringes were measured to be 0.25 nm, which can be attributed to the (311) plane of cubic Fe_3O_4 (JCPDS: 00-019-0629). In addition, after the immobilization of the nickel–PNP pincer complex, a significant change in the morphology of the Fe_3O_4@TiO_2 core–shell was not observed.

X-ray photoelectron spectroscopy (XPS)

The chemical and oxidation states of elements on the surface of Fe_3O_4@TiO_2 core–shell modified with immobilized nickel–PNP pincer complex (Fe_3O_4@TiO_2-PTES@NiPNP) were evaluated by XPS analysis. The XPS survey spectrum of the Fe_3O_4@TiO_2-

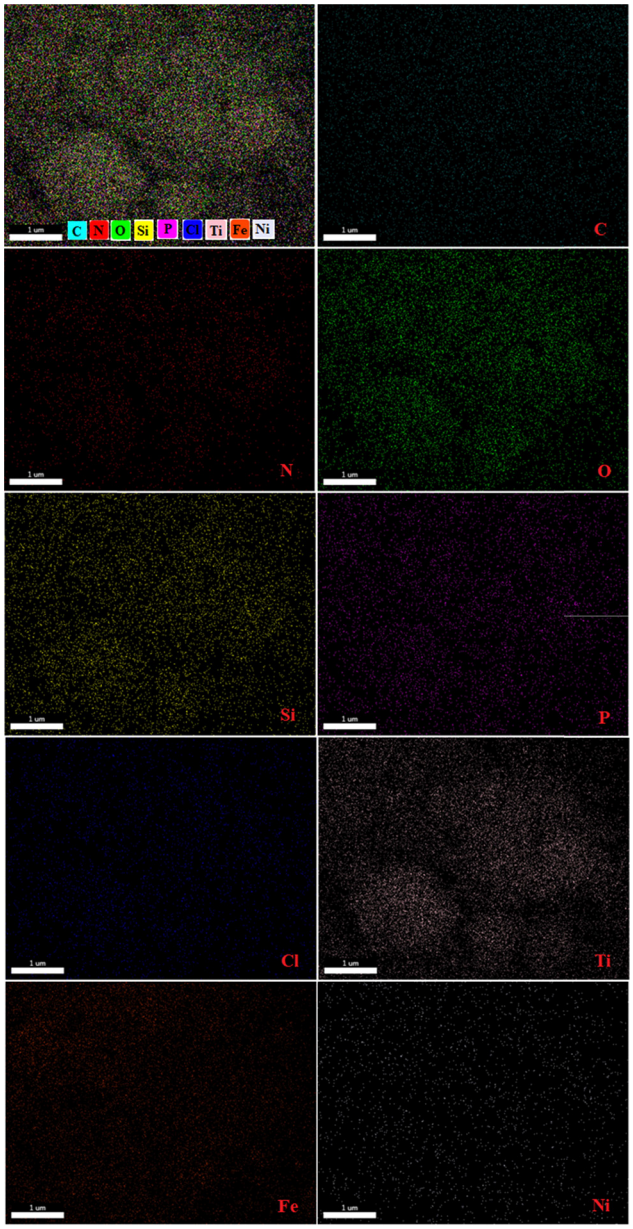

Fig. 7 EDS mapping images of Fe_3O_4@TiO_2-PTES@NiPNP; the immobilized nickel–PNP pincer complex onto the surface of the Fe_3O_4@TiO_2 core–shell.

PTES@NiPNP is depicted in Fig. 9(a), showing the characteristic binding energies of C 1s, Ti 2p, P 2p, Si 2p, Cl 2p, O 1s, N 1s, and Ni 2p. In the high-resolution spectrum of C 1s, the three peaks centered at 284.6, 285.9, and 287 eV are assigned to sp^2 and sp^3 carbon atoms in different chemical environments, such as carbon in C–C/C=C, C–N, and C=O (mainly carboxyl groups), respectively (Fig. 9(b)).[65,66] Furthermore, the existence of C=O possibly originates from the acetate group after hydrolysis onto Fe_3O_4 nanoparticles to prepare the Fe_3O_4@TiO_2 core–shell. Similarly, the high-resolution O 1s spectrum can be resolved into four peaks, which correspond to O_{vac}, Ti–O–Fe, C=O, and O–H with binding energies of 528.3, 531.1, 532.1, and 534.3 eV, respectively (Fig. 9(c)).[14,67,68] The oxygen

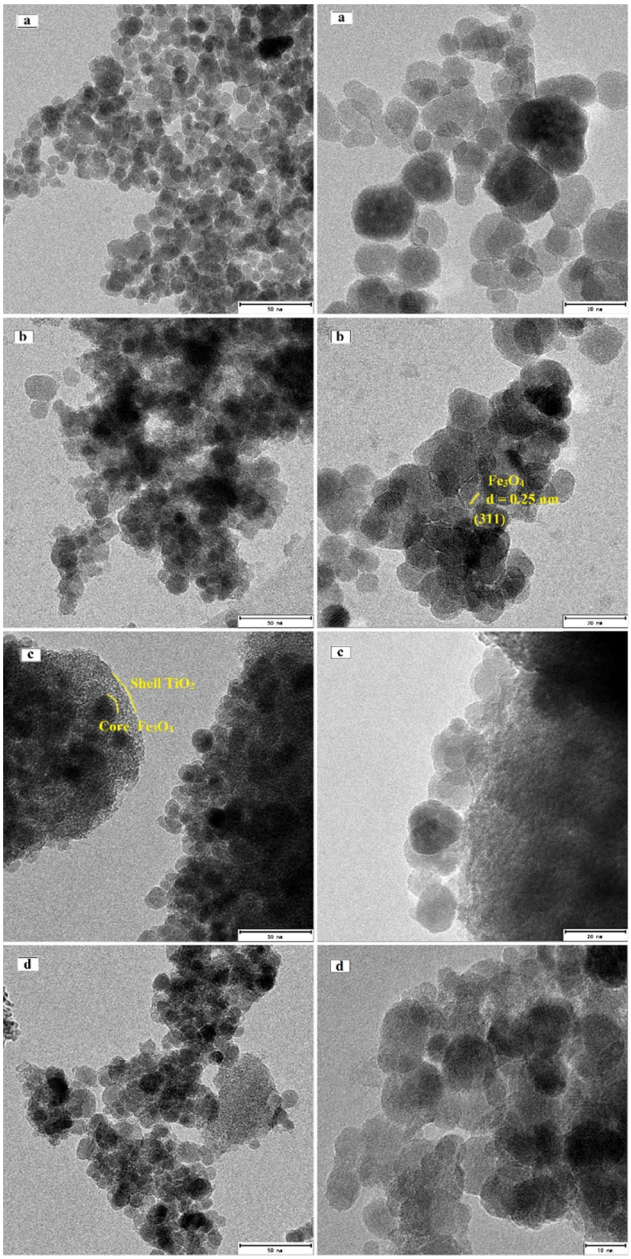

Fig. 8 TEM images of (a) Fe_3O_4, (b) Fe_3O_4@TiO_2, (c) Fe_3O_4@TiO_2-CPTES, and (d) Fe_3O_4@TiO_2-PTES@NiPNP.

vacancies can be attributed to the presence of structural defects in the amorphous shell of TiO_2 on Fe_3O_4 and to the coexistence of Ti^{3+}/Ti^{4+} states, which should be related to the partial loss of oxygen at the surface.[14,69] Consequently, the high-resolution XPS spectrum of Ti 2p exhibits two peaks at binding energies of 459.4 and 465.2 eV, which are attributed to Ti $2p_{3/2}$ and Ti $2p_{1/2}$, respectively. The difference in peak position (5.8 eV) indicates an oxidation state of Ti^{4+}.[70] Moreover, the peak at 463.2 eV belongs to Ti $2p_{1/2}$ associated with an oxidation state of Ti^{3+} (Fig. 9(d)).[70] The high-resolution Si 2p spectrum shown in Fig. 9(e) can be deconvoluted into four peaks at around 100.0, 102.4, 108.1, and 110 eV. These peaks are attributed to silicon in Si–C, Si–O_2, Si–OH, and Si–O–Si, respectively, confirming the successful functionalization of the Fe_3O_4@TiO_2 core–shell surface with CPTES.[71,72] The XPS spectrum of Ni 2p depicted in Fig. 9(f) exhibits two peaks at 856.9 and 863.2 eV, which are attributed to the binding energies of Ni $2p_{3/2}$, and two peaks at 874.4 and 880.2 eV, which are attributed to Ni $2p_{1/2}$, all of which can be indexed to the oxidation state of Ni^{2+} in the immobilized complex.[73,74] Moreover, in the Cl 2p spectrum, two characteristic peaks at 199.3 and 200.9 eV correspond well with Cl $2p_{3/2}$ and Cl $2p_{1/2}$, respectively, and indicate the presence of chlorine as Cl^- in the immobilized complex (Fig. S1).[75,76] From the TGA, CHN, XPS, and EDS-mapping analyses, it is clear that the immobilization of the nickel PNP pincer complex on the Fe_3O_4@TiO_2 core–shell surface is partially successful.

Argon sorption analysis

To gain information on the porous and surface properties of the Fe_3O_4, Fe_3O_4@TiO_2, and Fe_3O_4@TiO_2-CPTES nanostructures and the immobilized nickel–PNP pincer complex (Fe_3O_4@TiO_2-PTES@NiPNP), the argon adsorption–desorption isotherms were acquired at 87 K. The isothermal sorption plots of all the materials up to relative pressures near 0.99 are depicted in Fig. 10. The Fe_3O_4 nanoparticles exhibit a type-IVa isotherm with an H2(b) hysteresis loop (Fig. 10(a)), which is commonly characterized by the appearance of a plateau at high enough P/P_0 values.[77] However, in this case, the formed plateau is quite short and slightly ascending, which might suggest some type II characteristics. The appearance of its hysteresis suggests the occurrence of pore blockage, in which a wide distribution of pore diameters exists in the network.

For the other samples, the isotherms recorded, although still type IVa isotherms, seem to have a more type II character, as there is even less of a plateau at higher relative pressures, in addition to the rise in the adsorption isotherm being even more modest. Nonetheless, they show hysteresis loops albeit narrower than those found in the Fe_3O_4 nanoparticles, which may be classified as H4. This form of pore organization is typically found in mesoporous materials, where there is an overlap between monolayer and multilayer coverage. Additionally, the increased uptake at low pressures suggests the occurrence of micropores, which allows the isotherm to possess some type I character.[77]

The specific surface areas and total pore volumes for all samples were calculated using the Brunauer–Emmett–Teller (BET) theory and a single-point calculation acquired at P/P_0 near 0.99, respectively, as summarized in Table 2. The BET surface area of the amorphous TiO_2 precursor was previously reported as about 320 $m^2\ g^{-1}$.[20] After coating the Fe_3O_4 cores with an amorphous TiO_2 layer, the specific surface area and pore volume increased from 110 to 330 $m^2\ g^{-1}$ and 0.25 to 0.28 $cm^3\ g^{-1}$, respectively, indicating a uniform layer of amorphous TiO_2 on the surface of Fe_3O_4. As expected, after chloro functionalization and immobilization of the nickel–PNP pincer complex, the specific surface area and pore volume of the samples decreased to 320 and 270 $m^2\ g^{-1}$ and to 0.21 and 0.18 $cm^3\ g^{-1}$, respectively. This reduction in surface

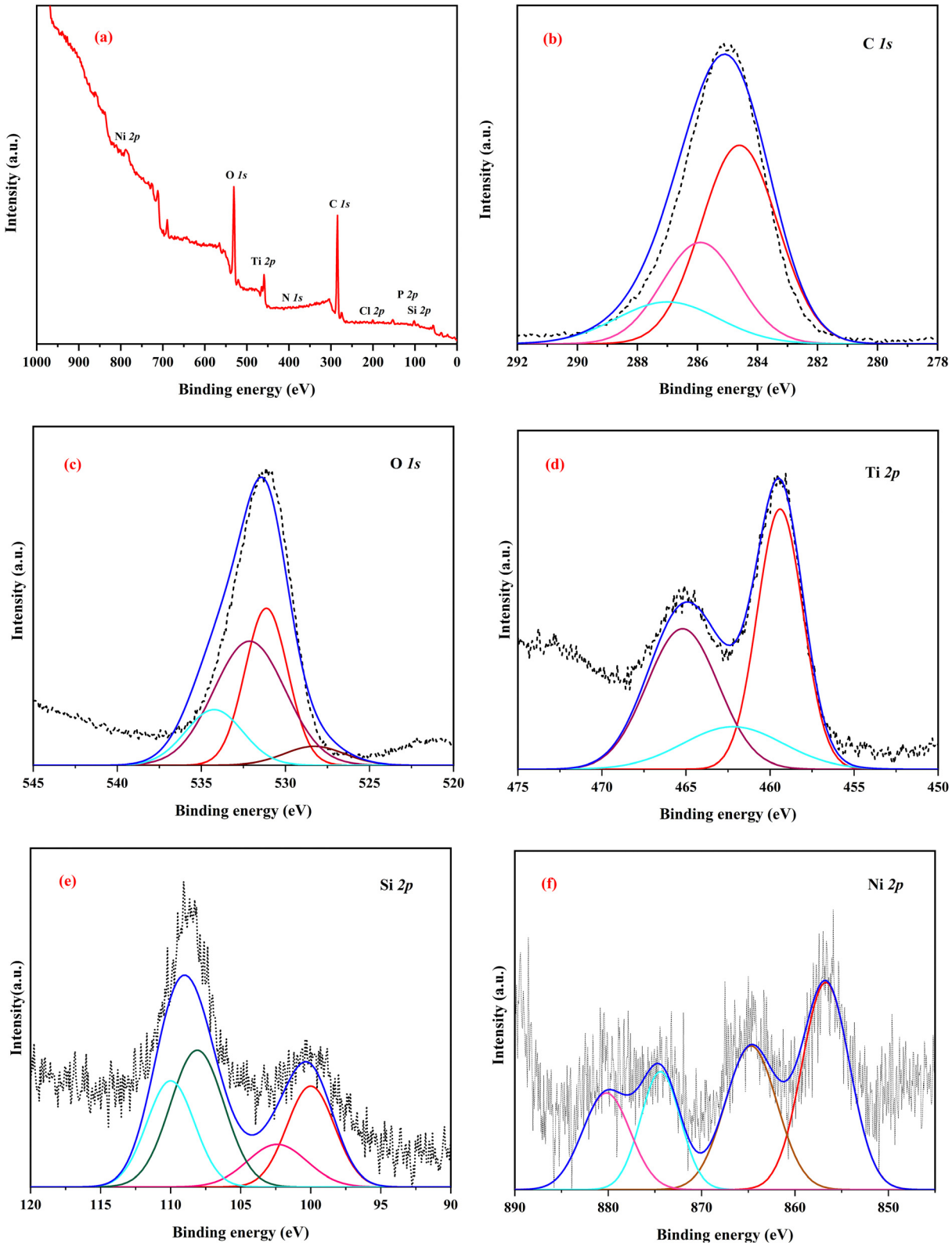

Fig. 9 (a) XPS survey spectra of Fe_3O_4@TiO_2-PTES@NiPNP. High-resolution XPS spectra of (b) C 1s, (c) O 1s, (d) Ti 2p, (e) Si 2p, and (f) Ni 2p.

area and pore volume is consistent with literature reports and can be attributed to the presence of additional chloropropyl groups and the immobilized nickel–PNP pincer complex on the internal and external pore surface of the Fe_3O_4@TiO_2 core–shell, restricting probe access during sorption experiments.[78]

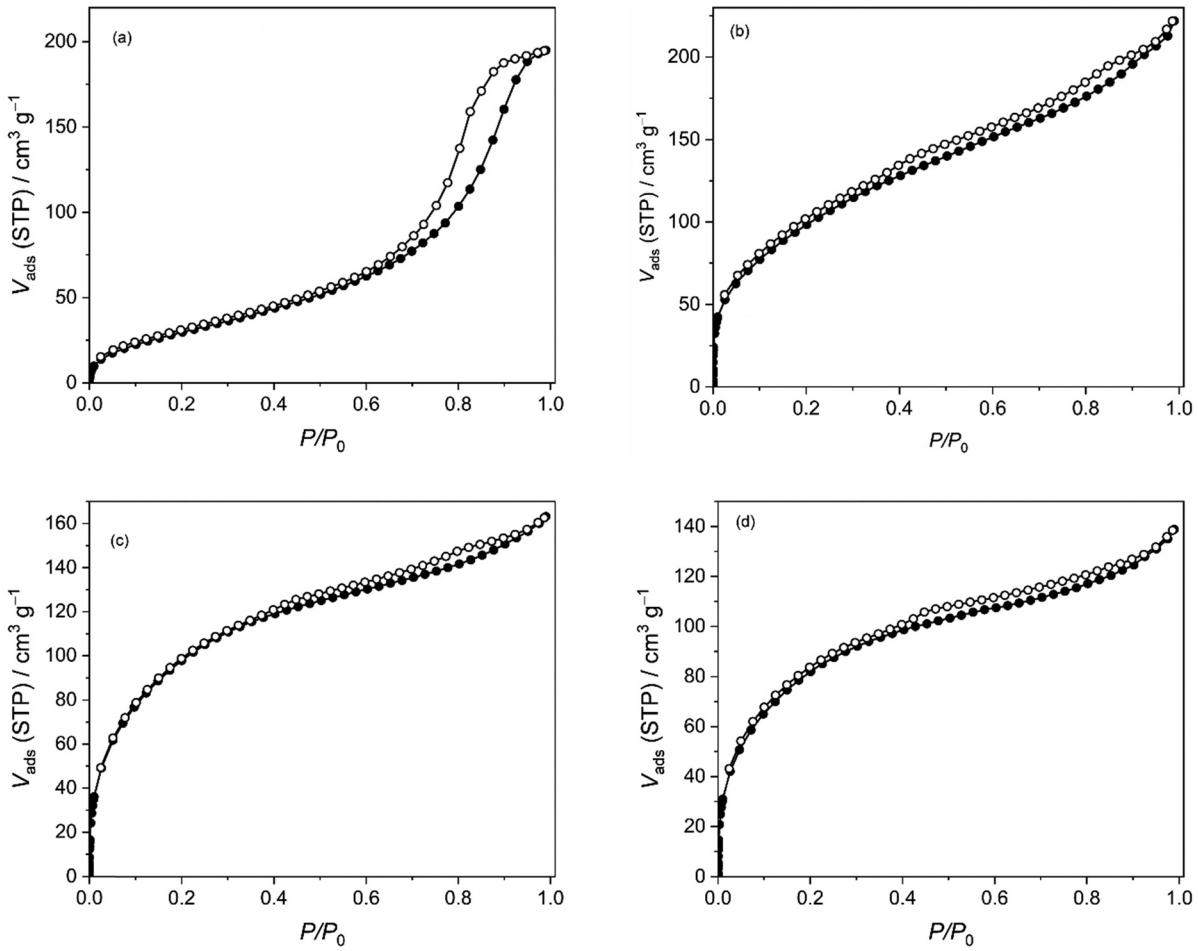

Fig. 10 Argon sorption isotherms for the (a) Fe_3O_4, (b) Fe_3O_4@TiO_2, (c) Fe_3O_4@TiO_2-CPTES nanostructures and (d) the immobilized nickel–PNP pincer complex at 87 K.

Table 2 Calculated BET surface areas and pore volumes for the Fe_3O_4, Fe_3O_4@TiO_2, Fe_3O_4@TiO_2-CPTES nanostructures and the material with the immobilized nickel–PNP pincer complex based on argon adsorption experiments at 87 K

Sample	BET (m^2 g^{-1})	P.V. (cm^3 g^{-1})
Fe_3O_4	110	0.25
Fe_3O_4@TiO_2	330	0.28
Fe_3O_4@TiO_2-CPTES	320	0.21
Fe_3O_4@TiO_2-PTES@NiPNP	270	0.18

To gain further insight into how immobilization affects pore size distribution, the isotherms were fitted using a non-local density functional theory (NLDFT) kernel based on adsorption models for argon on zeolites/silica at 87 K with cylindrical pores provided by Quantachrome Instruments.[43] The distribution plot for Fe_3O_4 shows that there is a much wider distribution of pore widths ranging from about 4 to 30 nm (Fig. 11a). This is consistent with the nature of H2(b) hysteresis. For the three functionalized materials, pore widths in the microporous range (<2 nm) were observed, which agrees with the type I character of their adsorption isotherm (Fig. 11b–d). This is consistent with the expected reduced access to the pores due to coating Fe_3O_4 with amorphous TiO_2 and successful immobilization of the nickel–PNP pincer complex onto the Fe_3O_4@TiO_2 core–shell surface.

Saturation magnetization experiments

Room temperature magnetization measurements were performed on the as-synthesized Fe_3O_4, Fe_3O_4@TiO_2, Fe_3O_4@TiO_2-CPTES nanostructures, and the material with immobilized nickel–PNP pincer complex using a vibrating sample magnetometer (VSM) with an applied field ranging from −10 to 10 kOe. The magnetization plots shown in Fig. 12 confirm the magnetic nature of all the materials and display saturation above 300 mT. The saturation magnetization (M_S) values for Fe_3O_4, Fe_3O_4@TiO_2, Fe_3O_4@TiO_2-CPTES nanostructures, and the material with the immobilized nickel–PNP pincer complex are approximately 53, 20, 18, and 15 emu g^{-1}, respectively.

The observed reduction in saturation magnetization correlates nicely with the relative increase in the non-magnetic component, *i.e.*, the amorphous TiO_2 shell on the surface of Fe_3O_4, as well as the introduction of chloropropyl groups and the immobilized nickel–PNP pincer complex. Among the four

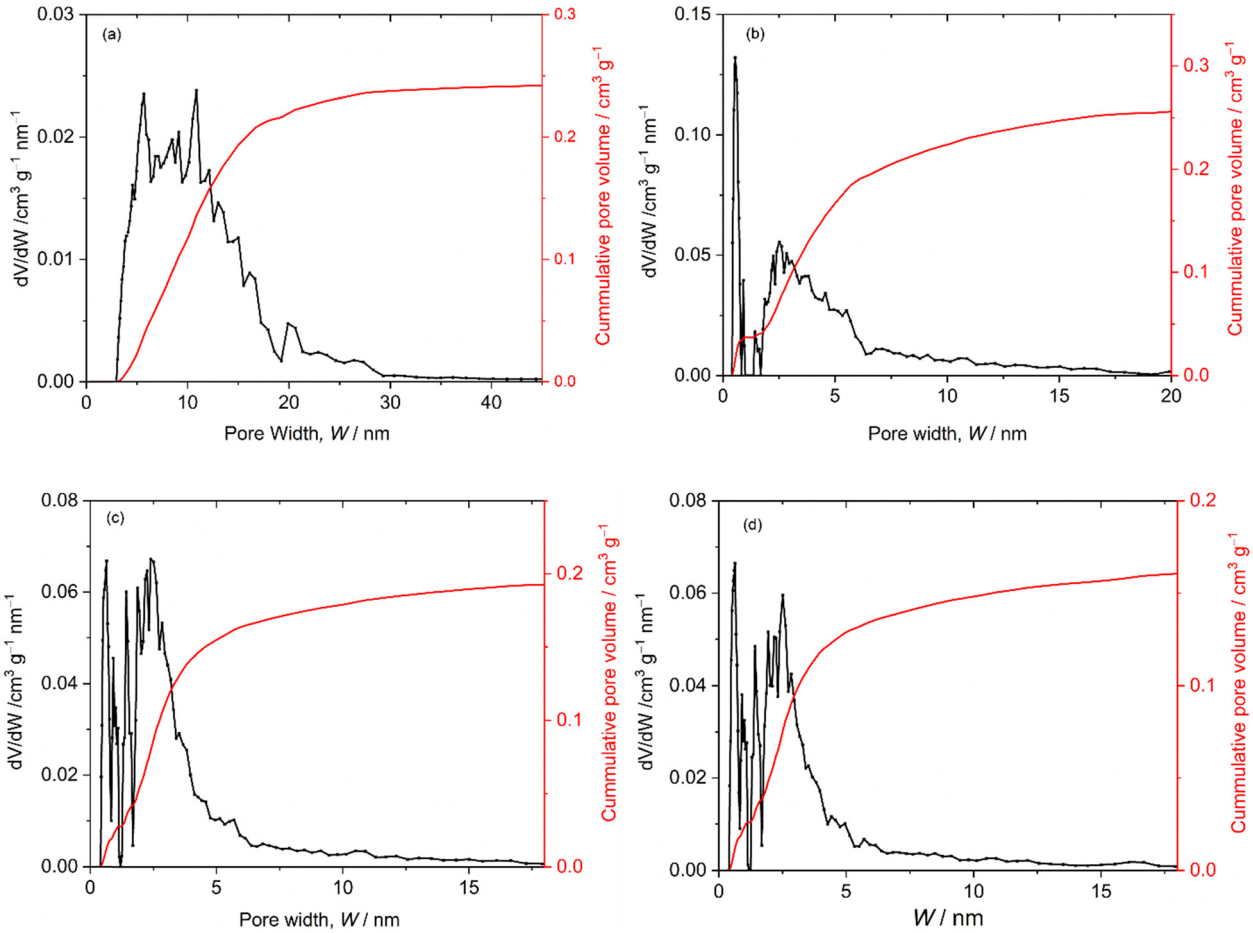

Fig. 11 Pore width distribution plots for (a) Fe_3O_4, (b) Fe_3O_4@TiO_2, (c) Fe_3O_4@TiO_2-CPTES nanostructures and (d) the immobilized nickel–PNP pincer complex obtained using a non-local density functional theory (NLDFT) kernel based on the adsorption models for argon on zeolites/silica at 87 K with cylindrical pores (see text for notation).

materials, only the Fe_3O_4 nanoparticles exhibit a significant hysteresis loop. Although the Fe_3O_4@TiO_2 and the material with the immobilized nickel–PNP pincer complex also display some forms of hysteresis, they exhibit lower coercivity and remnant magnetization values. Interestingly, the Fe_3O_4@TiO_2-CPTES nanostructure displays a butterfly shape with no remnant magnetization or coercivity. The observed hysteresis suggests that a reduction in magnetite content leads to a gradual diminution in the ordering of the iron centers. Consequently, the ability to retain magnetization is expected to decrease correspondingly. Overall, these results are consistent with the decreased Fe_3O_4 content stemming from the inclusion of TiO_2 and the subsequent immobilization of the pincer complex.

Antibacterial activities

The disc diffusion method was used to test the antimicrobial activity of the prepared Fe_3O_4, amorphous TiO_2, Fe_3O_4@TiO_2, and the immobilized nickel–PNP pincer complex (40 mg) against two types of *Staphylococcus aureus* and *Escherichia coli* bacteria. The antibacterial activities of synthesized nanostructures against pathogenic strains are displayed by measuring the inhibition zone (mm). As shown in Fig. 13, the immobilized nickel–PNP pincer complex on the surface of Fe_3O_4@TiO_2 core–shell was potentially effective in suppressing Gram-positive bacteria growth, while against Gram-negative bacteria growth, it did not have an inhibitory effect. The maximum zone of inhibition was observed against Gram-positive *Staphylococcus aureus* (19 mm), while the other nanostructures did not show any antibacterial activity against the two pathogenic strains of *Staphylococcus aureus* and *Escherichia coli* bacteria. The differences in the effects of the immobilized nickel–PNP pincer complex against *Escherichia coli* and *Staphylococcus aureus* may be derived from the structural differences in the cell walls of Gram-positive and Gram-negative bacteria and the electrostatic charge of the bacterial cell wall and nanostructures. According to recent reports, the mechanism of the antibacterial effect is that the nanostructures act as a positive charge, and the microbes act as a negative charge, creating an electrostatic attraction between the microbes and the surface of the nanostructure, resulting in damage to the bacterial cell wall.[79–81] Thus, the antibacterial action of the immobilized nickel–PNP pincer complex on the surface of Fe_3O_4@TiO_2 core–shell compared to other nanostructures indicates the excellent ability of

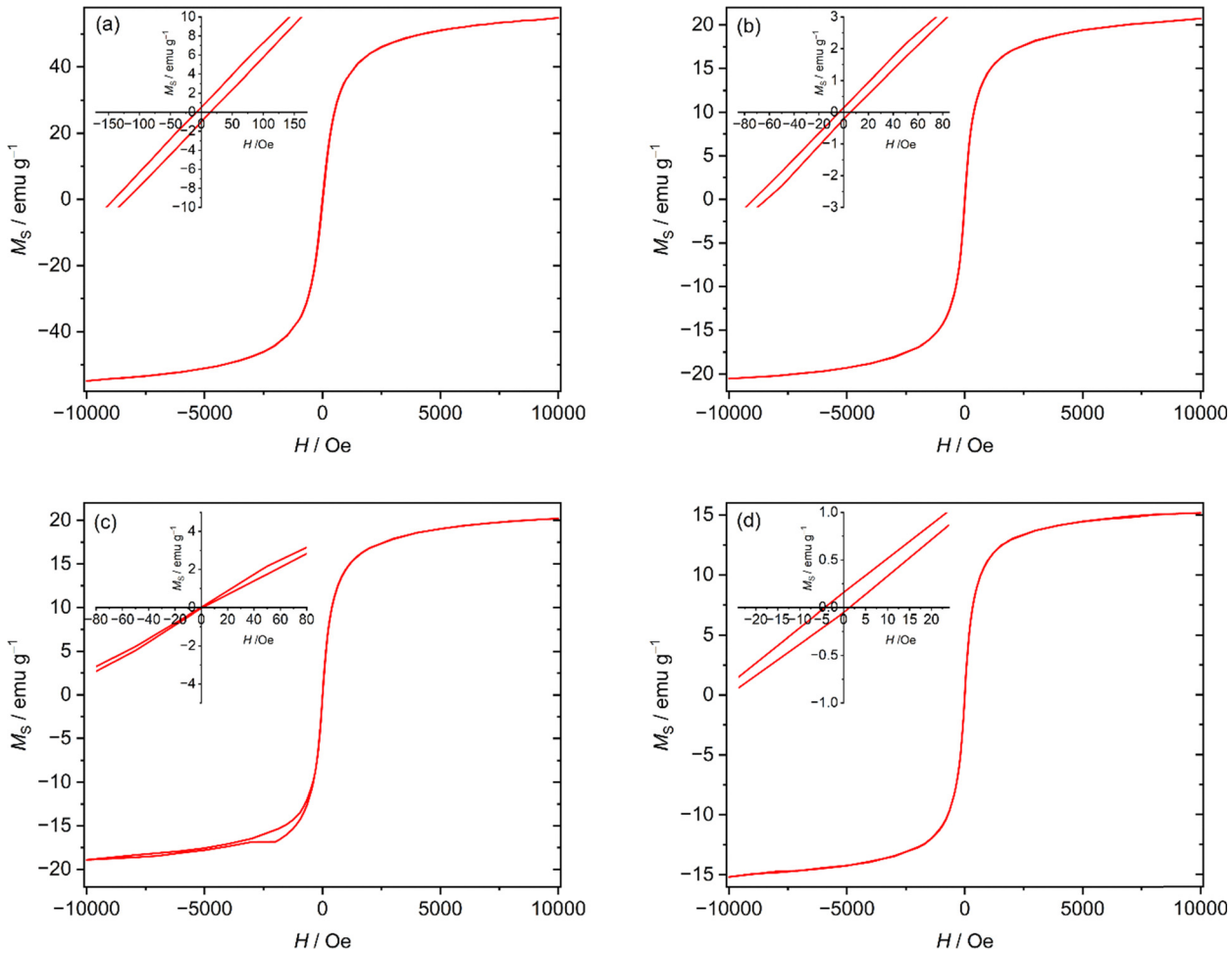

Fig. 12 Magnetization plots for the Fe_3O_4, Fe_3O_4@TiO_2, Fe_3O_4@TiO_2-CPTES nanostructures and the material with immobilized nickel–PNP pincer complex measured at room temperature (a)–(d), respectively. Insets: Zoomed-in view to display hysteresis loops.

this compound to be utilized as an antibacterial agent against pathogenic strains.

Electrochemical behavior of the modified GCEs

The electrochemical behaviors of the TiO_2 NPs, Fe_3O_4@TiO_2 core–shell, and Fe_3O_4@TiO_2-PTES@NiPNP hybrid were studied using cyclic voltammetry (CV). Fig. 14 illustrates the CV curve of the glassy carbon electrode (GCE) and modified GCEs in 0.1 M NaOH electrolyte at a scan rate of 100.0 mV s^{-1} and a potential range of 0–0.6 V. As shown in Fig. 14, the characteristics of CV curves are similar for GCE, TiO_2/GCE and Fe_3O_4@TiO_2/GCE, and no redox peaks were observed in the blank solution. Moreover, Fe_3O_4@TiO_2-PTES@NiPNP/GCE exhibits a pair of redox peaks with E_{pa} = 0.5 and E_{pc} = 0.42 assigned to the electron transfer of Ni^{2+}/Ni^{3+} redox couple *vs.* Ag/AgCl in the alkaline blank solution.[82] The results show that in TiO_2/GCE and Fe_3O_4@TiO_2/GCE, due to the poor electrical conductivity of TiO_2 NPs at room temperature, the electron transfer ability of the GCE electrode was weakened, and the redox peak was not observed.[83] Moreover, immobilizing nickel–PNP pincer complex onto the Fe_3O_4@TiO_2 surface as an electroactive substance leads to the improvement of the electron transfer ability in the electrode surface and observation of the electrical signal of the sensor.[84] Therefore, the prepared Fe_3O_4@TiO_2-PTES@NiPNP/GCE-modified electrode was used as a working electrode in all electrochemical measurements. To improve the adhesion of the hybrid system while maintaining long-term stability and biocompatibility, a conductive polymer or membrane, such as Nafion, was used. However, Nafion is known to adversely influence conductivity and electron transport to some extent.[85,86]

Response of Fe_3O_4@TiO_2-PTES@NiPNP/GCE to glucose

The electrochemical response of the Fe_3O_4@TiO_2-PTES@NiPNP/GCE as a function of glucose concentration is depicted in Fig. 15. After the addition of different concentrations of glucose (1, 10, 100, and 1000 μM), the Fe_3O_4@TiO_2-PTES@NiPNP/GCE electrode exhibits a remarkable increase for both anodic and cathodic peak current densities (ΔJ_{pa} = 1010 μA cm^{-2} and ΔJ_{pc} = 376 μA cm^{-2}, respectively), indicating the excellent electrocatalytic activity of Fe_3O_4@TiO_2-PTES@NiPNP for glucose oxidation in alkaline solution. In a neutral electrolyte, such as phosphate-buffered saline (PBS), the absence of hydroxyl ions required for the generation of Ni^{3+} species inhibits the interaction between nickel and glucose; consequently, the

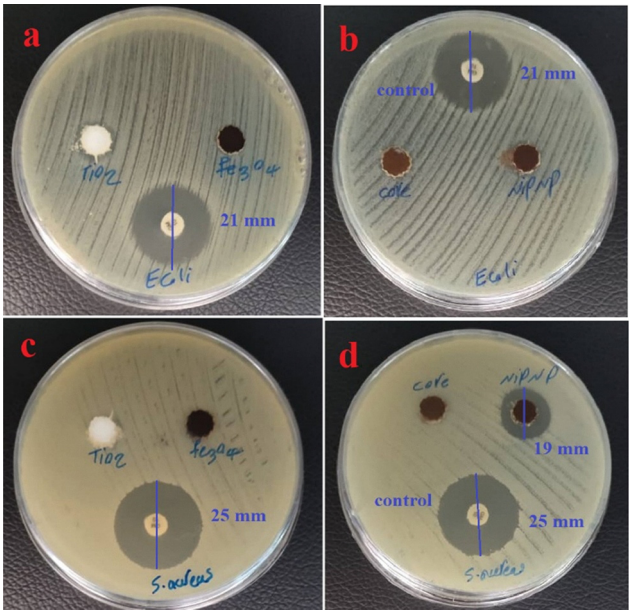

Fig. 13 Zone of inhibition observed against *E. coli* (a), (b) and *S. aureus* (c), (d) for Fe_3O_4, amorphous TiO_2, Fe_3O_4@ TiO_2 core–shell and the immobilized nickel–PNP pincer complex.

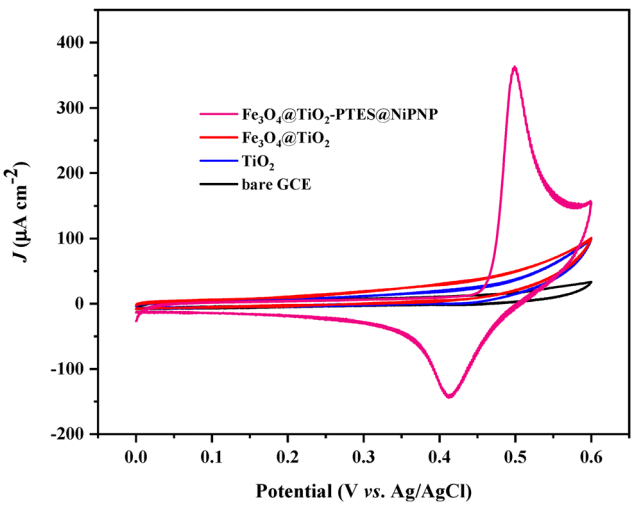

Fig. 14 Cyclic voltammograms of the bare GCE, TiO_2 nanostructure/GCE, Fe_3O_4@TiO_2 core–shell/GCE, and Fe_3O_4@TiO_2-PTES@NiPNP hybrid/GCE in 0.1 M NaOH at a scan rate of 100 mV s^{-1}.

modified electrode is not active toward glucose oxidation in a neutral solution.[87] The oxidation of glucose to gluconolactone is catalyzed by the Ni(III)/(II) redox couple according to the following reaction mechanism:

$$Ni^{II} + OH^- \rightarrow Ni^{III} + e^-$$

$$Ni^{III} + \text{glucose} \rightarrow Ni^{II} + \text{gluconolactone}$$

In the initial electrochemical recognition processes, after the adsorption of glucose on the modified electrode, the Ni^{II} species were first oxidized to Ni^{III} species in an alkaline solution on the

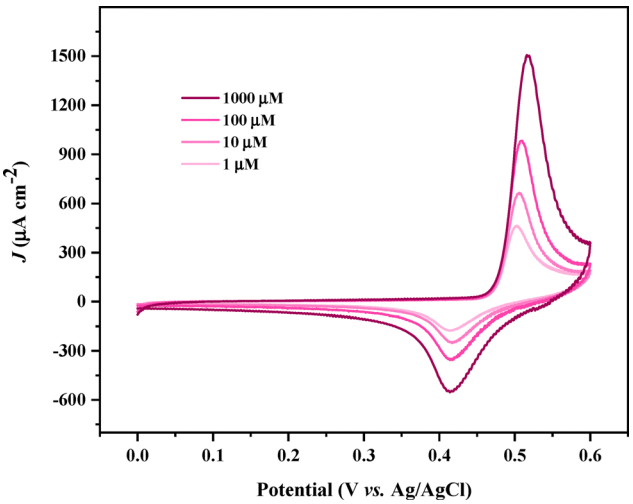

Fig. 15 Cyclic voltammograms of the Fe_3O_4@TiO_2-PTES@NiPNP/GCE with Nafion in the presence of different concentrations of glucose (1, 10, 100, and 1000 μM) and 0.1 M NaOH at a scan rate of 100 mV s^{-1}.

electrode surface. Pre-adsorbed glucose was then oxidized to gluconolactone by the reduction of Ni^{III} species, resulting in the simultaneous regeneration of the Ni^{II} species.[85,86]

In order to review the reaction kinetics of the Fe_3O_4@TiO_2-PTES@NiPNP/GCE electrode surface, CV curves were recorded with Nafion in 0.1 M NaOH electrolyte containing 0.1 mM glucose at different scan rates (30–300 mV s^{-1}). Fig. 16(a) illustrates that the anodic peak (J_{pa}) shifts towards more positive values and the cathodic peak (J_{pc}) moves towards more negative values with the increase in scan rate.[82] The result shows that the current densities of both the anodic and cathodic peaks increase linearly with the scan rate, indicating that the electrochemical catalytic process on the Fe_3O_4@TiO_2-PTES@NiPNP/GCE electrode surface is a diffusion-controlled process, which is ideal for the quantitative analysis of glucose determination (Fig. 16(b)).[82]

To study the accurate qualification of the Fe_3O_4@TiO_2-PTES@NiPNP/GCE electrode for glucose detection and to numerically investigate its detection limit and sensitivity, differential pulse voltammetry (DPV) measurements were carried out at various concentrations of glucose. DPV was used as a highly sensitive electrochemical technique for glucose detection. Fig. 17(a) shows the DPV of the Fe_3O_4@TiO_2-PTES@NiPNP/GCE electrode at different glucose concentrations ranging from 5 μM to 7 mM in 0.1 M NaOH, which is a wide range with high sensitivity and low detection limit. Fig. 17(b) shows its corresponding calibration curve as linear ranging from 5 μM to 0.1 mM and 0.1 mM to 7 mM glucose concentrations following the regression equations of $J_p = 3.69\ C_{glu} + 584.74$ ($R^2 = 0.944$) and $J_p = 0.28\ C_{glu} + 1042.68$ ($R^2 = 0.989$) (C_{glu}: glucose concentration, μM, and J_p: peak current density, μA cm^{-2}).

According to the data, the detection limit is calculated to be 0.894 μM (S/N = 3), while the sensitivities for the 5 μM–0.1 mM and 0.1 mM–7 mM ranges are 3692 and 276 μA mM^{-1} cm^{-2}, respectively. As observed, with increasing glucose concentration,

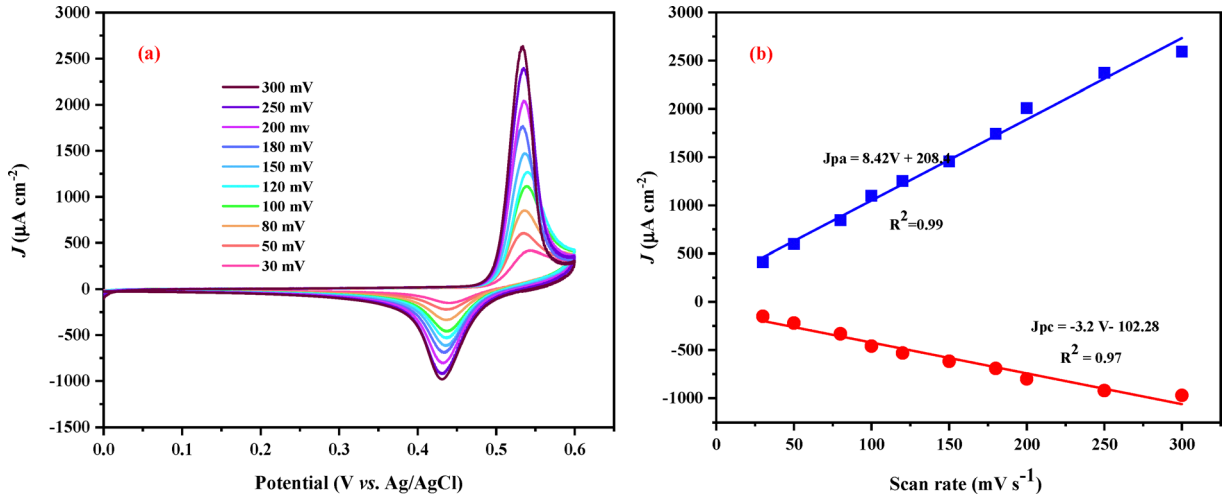

Fig. 16 (a) Cyclic voltammograms of the Fe_3O_4@TiO_2-PTES@NiPNP/GCE with Nafion in the presence of 0.1 mM glucose and 0.1 M NaOH at different scan rates of 30–300 mV. s^{-1}. (b) the linear plots of Ni(III)/(II) redox peak current density *vs.* scan rates.

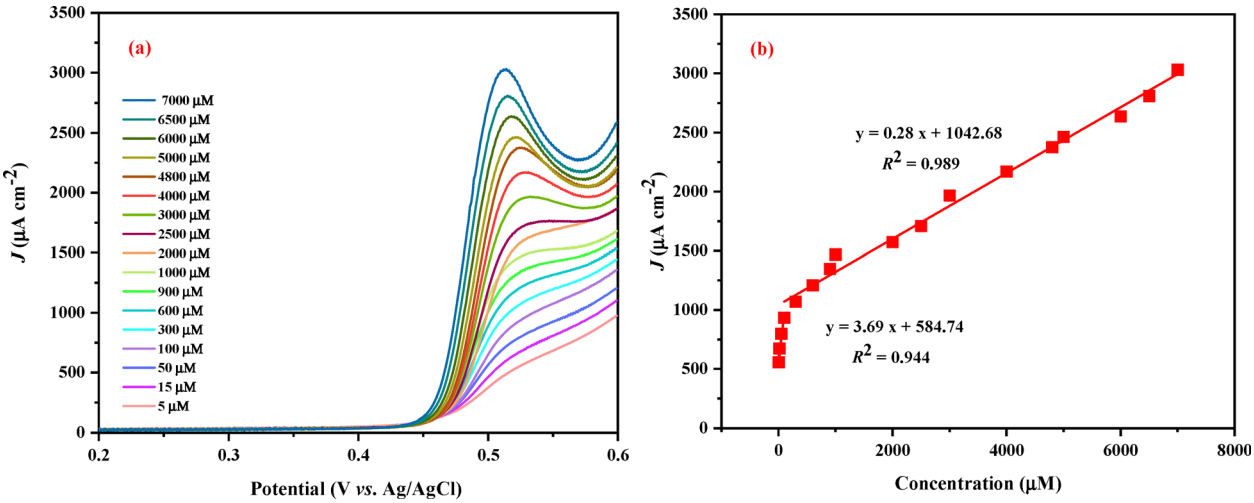

Fig. 17 (a) DPV diagrams of the Fe_3O_4@TiO_2-PTES@NiPNP/GCE with Nafion at different glucose concentrations in 0.1 M NaOH; (b) its corresponding calibration curve (for 5–2500 μM, the *J* values were acquired at +0.525 V).

the calibration curve deviates from linearity, accompanied by a noticeable decrease in sensor sensitivity. This behavior can be attributed to the adsorption and accumulation of electrocatalytic reaction intermediates (such as gluconolactone) on the electrode surface. The adsorbed species hinder the diffusion of glucose molecules and hydroxide ions toward the electroactive sites, leading to blockage and eventual saturation of the catalytically active sites.[85] Compared with glucose sensors reported in the

Table 3 Comparison of the analytical performance of the Fe_3O_4@TiO_2-PTES@NiPNP/Nafion-modified electrode with some previously reported nickel-based nonenzymatic glucose sensors

Electrode	Linear range	Limit of detection	Sensitivity	Ref.
NiONF-rGO	2.0 μM–0.60 mM	0.77 μM (S/N = 3)	1100 μA mM^{-1} cm^{-2}	88
CPO-27-Ni^{II}	0.04–6 mM	1.46 μM (S/N = 3)	40.95 μA mM^{-1}	89
$NiCeO_x$/MWCNTs	0.007–0.466 mM, 0.466–3.44 mM	1.8 μM (S/N = 3)	271.53, 429.95 μA mM^{-1} cm^{-2}	90
NiO HHs	0.1–5 μM	1.2 μM (S/N = 3)	1052.8 μA mM^{-1} cm^{-2}	91
NiO/Pt/ERGO	0.05–5.66 mM	0.2 μM (S/N = 3)	668.2 μA mM^{-1} cm^{-2}	92
Ni/NiO-rGO	0.03–6.44 mM	1.8 μM (S/N = 3)	1997 μA mM^{-1} cm^{-2}	93
Ni(PDA)MOF@CNF	10–3000 μM	0.053 μM (S/N = 3)	9457.5 μA mM^{-1} cm^{-2}	94
NiO/SiC	0.004–7.5 mM	0.32 μM (S/N = 3)	2.037 mA mM^{-1} cm^{-2}	95
Fe_3O_4@TiO_2-PTES@NiPNP	5 μM–0.1 mM, 0.1 mM–7 mM	0.894 μM (S/N = 3)	3692 μA mM^{-1} cm^{-2} 276 μA mM^{-1} cm^{-2}	This work

literature (Table 3), the Fe_3O_4@TiO_2-PTES@NiPNP-based sensor in the presence of Nafion exhibits comparable performance, showing lower detection limits and satisfactory sensitivity. We believe this might be due to the synergistic effects of the Ni–PNP aliphatic pincer complex and the Fe_3O_4@TiO_2 support. Furthermore, the unique structure of Fe_3O_4@TiO_2-PTES@NiPNP with its high specific surface area, controllable morphology, and architecture of support, in addition to the presence of a Ni complex, functions to effectively increase the electrochemical specific surface area of the hybrid and reduce the electron transfer resistance, which is overall beneficial. As a result, the existence of many catalytically active sites in a hybrid structure to accommodate glucose molecules is expected to improve the range of linearity for glucose molecule detection.

Conclusions

In summary, a hybrid material based on the Fe_3O_4@TiO_2 core–shell with an immobilized aliphatic nickel–PNP pincer complex was successfully fabricated by multistep synthesis. The Fe_3O_4@TiO_2 core–shell structure was prepared as a support by the hydrolysis of titanium(IV) ethoxide in a mixture of ethanol, acetic acid, and water with molar ratios (1 : 25 : 0.1 : 4) on the surface Fe_3O_4 core at reflux temperature. The core–shell morphology, band gap, magnetization, and surface area could be controlled by hydrolysis, and these physical characteristics changed after immobilizing the aliphatic nickel–PNP pincer complex. The immobilized aliphatic nickel–PNP pincer complex shows high antibacterial activity (maximum zone of inhibition 19 mm) against Gram-positive pathogenic strains compared to other samples due to an electrostatic attraction between the microbes (negative charge) and the immobilized aliphatic nickel–PNP pincer complex (positive charge), which leads to damage to the bacterial cell wall. Finally, the modified electrode with the immobilized aliphatic nickel–PNP pincer complex exhibited a wide linear range of 5 μM to 0.1 mM and 0.1 to 7 mM and high sensitivities of 3692 and 276 μA mM^{-1} cm^{-2} with a low detection limit of 0.894 μM (S/N = 3) in the alkaline medium for nonenzymatic glucose determination. The suitable performance of the sensor is attributed to its unique hybrid structure, such as its high surface area and rich redox-active sites for charge transfer and glucose oxidation.

Author contributions

F. A., investigation, visualization, writing the original draft; G. M., funding acquisition, supervision, data curation, visualization, writing – review and editing; O. A., investigation, data curation, visualization, writing – review and editing; and W. P., funding acquisition, supervision, data curation, visualization, writing – review and editing.

Conflicts of interest

There are no conflicts to declare.

Data availability

The data supporting this article have been included as part of the supplementary information (SI). Supplementary information is available. See DOI: https://doi.org/10.1039/d5ma00762c.

Acknowledgements

This work is based upon the research funded by the Iran National Science Foundation (INSF) under project No 4037569, the Research Affairs Division of Isfahan University of Technology (IUT) and the Deutsche Forschungsgemeinschaft (PL 155/26-1).

References

1 N. Cutillas, G. S. Yellol, C. de Haro, C. Vicente, V. Rodríguez and J. Ruiz, Anticancer cyclometalated complexes of platinum group metals and gold, *Coord. Chem. Rev.*, 2013, **257**, 2784–2797, DOI: 10.1016/j.ccr.2013.03.024.

2 G. Mohammadnezhad, S. Abad, H. Farrokhpour, H. Görls and W. Plass, Electrocatalytic property, anticancer activity, and density functional theory calculation of [NiCl (P^N^P)] Cl. EtOH, *Appl. Organomet. Chem.*, 2021, **35**, e6092, DOI: 10.1002/aoc.6092.

3 B. K. Tate, C. M. Wyss, J. Bacsa, K. Kluge, L. Gelbauma and J. P. Sadighi, A dinuclear silver hydride and an umpolung reaction of CO_2, *Chem. Sci.*, 2013, **4**, 3068–3074, DOI: 10.1039/c3sc50896j.

4 H. Tavallali, G. Deilamy-Rad, A. Moaddeli and K. Asghari, A new pincer-type ''naked-eye'' colorimetric probe for Cu^{2+} determination in 80% water media and its application as a solid state sensor and an efficient antibacterial product, *Sens. Actuators, B*, 2017, **244**, 1121–1128, DOI: 10.1016/j.snb.2016.11.114.

5 M. C. Tang, M. Y. Leung, S. L. Lai, M. Ng, M. Y. Chan and V. Wing-Wah Yam, Realization of thermally stimulated delayed phosphorescence in aryl gold(III) complexes and efficient gold(III) based blue-emitting organic light-emitting devices, *J. Am. Chem. Soc.*, 2018, **140**, 13115–13124, DOI: 10.1021/jacs.8b09205.

6 S. Kar, R. Sen, A. Goeppert and G. S. Prakash, Integrative CO_2 capture and hydrogenation to methanol with reusable catalyst and amine: toward a carbon neutral methanol economy, *J. Am. Chem. Soc.*, 2018, **140**, 1580–1583, DOI: 10.1021/jacs.7b12183.

7 E. Fogler, E. Balaraman, Y. Ben-David, G. Leitus, L. J. Shimon and D. Milstein, New CNN-type ruthenium pincer NHC complexes. Mild, efficient catalytic hydrogenation of esters, *Organometallics*, 2011, **30**, 3826–3833, DOI: 10.1021/om200367j.

8 P. Gao, G. Liang, T. Ru, X. Liu, H. Qi, A. Wang and F. E. Chen, Phosphorus coordinated Rh single-atom sites on nanodiamond as highly regioselective catalyst for hydroformylation of olefins, *Nat. Commun.*, 2021, **12**, 4698, DOI: 10.1038/s41467-021-25061-0.

9 M. Esfandiari, G. Havaei, S. Zahiri and G. Mohammadnezhad, Pincer complex immobilization onto different supports: Strategies and applications, *Coord. Chem. Rev.*, 2022, **472**, 214778, DOI: 10.1016/j.ccr.2022.214778.

10 M. Ngcobo and S. O. Ojwach, Ethylene oligomerization reactions catalyzed by recyclable Fe(II), Ni(II) and Co(II) complexes immobilized on Fe_3O_4 magnetic nanoparticles, *Mol. Catal.*, 2021, **508**, 111583, DOI: 10.1016/j.mcat.2021.111583.

11 D. Sengupta, L. Radhakrishna and M. S. Balakrishna, Synthesis of Indoles and Benzofurans Using a Graphene Oxide-Grafted Aminobisphosphine–Pd^{II} Complex, *ACS Omega*, 2018, **3**, 15018–15023, DOI: 10.1021/acsomega.8b02120.

12 L. Alrais, S. S. Gholap, I. Dutta, E. Abou-Hamad, B. W. Chen, J. Zhang, M. N. Hedhili, J. M. Basset and K. W. Huang, Highly efficient immobilized PN^3P-pincer iridium catalyst for dehydrogenation of neat formic acid, *Appl. Catal., B*, 2024, **342**, 123439, DOI: 10.1016/j.apcatb.2023.123439.

13 M. J. Kramer, M. B. Leonard, J. Ruan, D. E. Lai, P. Y. Zavalij, E. E. Rodriguez and A. N. Vedernikov, Mesoporous Silica Nanoparticle Rigid Anchor Attached Pt Complex for Catalytic H/D Exchange of Aromatic Substrates, *Inorg. Chem.*, 2025, **64**, 1994–2005, DOI: 10.1021/acs.inorgchem.4c04792.

14 M. Esfandiari, G. Mohammadnezhad, O. Akintola, F. Otto, T. Fritz and W. Plass, Sustainable catalysts for efficient triazole synthesis: an immobilized triazine-based copper-NNN pincer complex on TiO_2, *Dalton Trans.*, 2023, **52**, 11875–11885, DOI: 10.1039/d3dt02118a.

15 W. Chen, P. Cai, H. C. Zhou and S. T. Madrahimov, Bridging Homogeneous and Heterogeneous Catalysis: Phosphine-Functionalized Metal–Organic Frameworks, *Angew. Chem., Int. Ed.*, 2024, **63**, e202315075, DOI: 10.1002/anie.202315075.

16 R. Kumar, T. Mandal, A. Bhattacherya, M. K. Pandey, J. K. Bera and J. Choudhury, Hyper-Cross-Linked Polymer-Based Self-Supported Reusable RuNHC Catalyst for Amine-Assisted Hydrogenation of CO_2 to Methanol, *ACS Catal.*, 2024, **14**, 13236–13245, DOI: 10.1021/acscatal.4c02513.

17 J. S. Serrano-García, M. A. García-Eleno, A. Arenaza-Corona, E. Rufino-Felipe, H. Valdés, S. Hernandez-Ortega and D. Morales-Morales, Simple and easy functionalization of *para*-hydroxy POCOP-M (M = Ni(II), Pd(II)) pincer complexes: synthesis of multimetallic species, *Dalton Trans.*, 2025, **54**, 694–699, DOI: 10.1039/D4DT02841D.

18 J. Zheng, Y. Wu, Q. Zhang, Y. Li, C. Wang and Y. Zhou, Direct liquid phase deposition fabrication of waxberry-like magnetic Fe_3O_4@TiO_2 core-shell microspheres, *Mater. Chem. Phys.*, 2016, **181**, 391–396, DOI: 10.1016/j.matchemphys.2016.06.074.

19 M. Ardani, M. Imani and A. Tadjarodi, Core shell Fe_3O_4@-TiO_2/silica aerogel nanocomposite; synthesis and study of structural, magnetic and photocatalytic properties, *Microporous Mesoporous Mater.*, 2022, **338**, 111757, DOI: 10.1016/j.micromeso.2022.111757.

20 F. Ariaeinezhad, G. Mohammadnezhad, M. Zare, O. Akintola and W. Plass, Controllable and facile one-pot synthesis of high surface area amorphous, crystalline, and triphasic TiO_2: catalytic and photocatalytic applications, *J. Mater. Chem. A*, 2024, **12**, 6488–6506, DOI: 10.1039/D3TA07610E.

21 F. Mushtaq, X. Chen, S. Staufert, H. Torlakcik, X. Wang, M. Hoop, A. Gerber, X. Li, J. Cai, B. J. Nelson and S. Pané, On-the-fly catalytic degradation of organic pollutants using magneto-photoresponsive bacteria-templated microcleaners, *J. Mater. Chem. A*, 2019, **7**, 24847–24856, DOI: 10.1039/C9TA06290D.

22 N. Geng, W. Chen, H. Xu, T. Lin, M. Ding, Y. Wang, H. Tao and K. Hu, Preparation of Fe_3O_4/TiO_2-N-GO sonocatalyst and using for humic acid removal with the assist of ultrasound, *Mater. Sci. Semicond. Process.*, 2019, **102**, 104593, DOI: 10.1016/j.mssp.2019.104593.

23 S. H. Hosseini, N. Zohreh, S. Alipour, C. Busuioc and R. Negrea, Gold nanoparticles stabilized on SBA-15 functionalized NNN-pincer ligand; highly effective catalyst for reduction of nitroarenes in aqueous medium, *Catal. Commun.*, 2018, **108**, 93–97, DOI: 10.1016/j.catcom.2018.01.002.

24 L. R. Kalankesh, S. Rodríguez-Couto, M. A. Zazouli, Y. D. Shahamat, R. A. Dianati and M. Arghiani, Synthesis and characterization of nanoparticles and composites as bactericides, *J. Microbiol. Methods*, 2019, **167**, 105736, DOI: 10.1016/j.mimet.2019.105736.

25 B. Vaferi, M. Bahmani, P. Keshavarz and D. Mowla, Experimental and theoretical analysis of the UV/H_2O_2 advanced oxidation processes treating aromatic hydrocarbons and MTBE from contaminated synthetic wastewaters, *J. Environ. Chem. Eng.*, 2014, **2**, 1252–1260, DOI: 10.1016/j.jece.2014.05.016.

26 Y. Lee, L. Kovalova, C. S. McArdell and U. von Gunten, Prediction of micropollutant elimination during ozonation of a hospital wastewater effluent, *Water Res.*, 2014, **64**, 134–148, DOI: 10.1016/j.watres.2014.06.027.

27 K. Szymanska, A. I. Zouboulis and D. Zamboulis, Hybrid ozonation–microfiltration system for the treatment of surface water using ceramic membrane, *J. Membr. Sci.*, 2014, **468**, 163–171, DOI: 10.1016/j.memsci.2014.05.056.

28 Z. Chen, H. H. Ngo and W. Guo, A critical review on sustainability assessment of recycled water schemes, *Sci. Total Environ.*, 2012, **426**, 13–31, DOI: 10.1016/j.scitotenv.2012.03.055.

29 B. Li and T. Zhang, Different removal behaviours of multiple trace antibiotics in municipal wastewater chlorination, *Water Res.*, 2013, **47**, 2970–2982, DOI: 10.1016/j.watres.2013.03.001.

30 M. A. Zazouli and L. R. Kalankesh, Removal of precursors and disinfection byproducts (DBPs) by membrane filtration from water; a review, *J. Environ. Health Sci. Eng.*, 2017, **15**, 1–10, DOI: 10.1186/s40201-017-0285-z.

31 P. Nagarasu, P. Gayathri, S. N. Sri, N. Saisubramanian, P. Dhanaraj, D. Moon, S. P. Anthony and V. Madhu, Synthesis, antibiofilm activity and molecular docking study of new water-soluble copper(II)–pincer complexes, *Inorg. Chem. Commun.*, 2022, **139**, 109316, DOI: 10.1016/j.inoche.2022.109316.

32 A. Aragón-Muriel, V. Reyes-Márquez, F. Cañavera-Buelvas, J. R. Parra-Unda, F. Cuenú-Cabezas, D. Polo-Cerón, R. Colorado-Peralta, G. V. Suárez-Moreno, B. A. Aguilar-Castillo and

D. Morales-Morales, *Inorganics*, 2022, **10**, 134, DOI: 10.3390/inorganics10090134.

33 S. N. Shukla, P. Gaur, M. L. Raidas, B. Chaurasia and S. S. Bagri, Novel NNO pincer type Schiff base ligand and its complexes of Fe(III), Co(II) and Ni(II): Synthesis, spectroscopic characterization, DFT, antibacterial and anticorrosion study, *J. Mol. Struct.*, 2021, **1240**, 130582, DOI: 10.1016/j.molstruc.2021.130582.

34 A. Das, R. Sangavi, S. Gowrishankar, R. Kumar and M. Sankaralingam, Deciphering the Mechanism of MRSA Targeting Copper(II) Complexes of NN_2 Pincer-Type Ligands, *Inorg. Chem.*, 2023, **62**, 18926–18939, DOI: 10.1021/acs.inorgchem.3c02480.

35 D. E. Camporotondi, M. L. Foglia, G. S. Alvarez, A. M. Mebert, L. E. Diaz, T. Coradin and M. F. Desimone, Antimicrobial properties of silica modified nanoparticles, *Microb. Pathog. Strateg. Combat. Them. Sci. Technol. Educ.*, 2013, **2**, 283–290.

36 Y. Su, H. Guo, Z. Wang, Y. Long, W. Li and Y. Tu, Au@ Cu_2O core-shell structure for high sensitive nonenzymatic glucose sensor, *Sens. Actuators, B*, 2018, **255**, 2510–2519, DOI: 10.1016/j.snb.2017.09.056.

37 Y. Shu, T. Su, Q. Lu, Z. Shang, Q. Xu and X. Hu, Highly stretchable wearable electrochemical sensor based on Ni-Co MOF nanosheet-decorated Ag/rGO/PU fiber for continuous sweat glucose detection, *Anal. Chem.*, 2021, **93**, 16222–16230, DOI: 10.1021/acs.analchem.1c04106.

38 L. Wang, Y. Zhang, Y. Xie, J. Yu, H. Yang, L. Miao and Y. Song, Three-dimensional macroporous carbon/hierarchical Co_3O_4 nanoclusters for nonenzymatic electrochemical glucose sensor, *Appl. Surf. Sci.*, 2017, **402**, 47–52, DOI: 10.1016/j.apsusc.2017.01.062.

39 W. He, Y. Sun, J. Xi, A. A. M. Abdurhman, J. Ren and H. Duan, Printing graphene-carbon nanotube-ionic liquid gel on graphene paper: towards flexible electrodes with efficient loading of PtAu alloy nanoparticles for electrochemical sensing of blood glucose, *Anal. Chim. Acta*, 2016, **903**, 61–68, DOI: 10.1016/j.aca.2015.11.019.

40 A. Abellán-Llobregat, I. Jeerapan, A. Bandodkar, L. Vidal, A. Canals, J. Wang and E. Morallon, A stretchable and screen-printed electrochemical sensor for glucose determination in human perspiration, *Biosens. Bioelectron.*, 2017, **91**, 885–891, DOI: 10.1016/j.bios.2017.01.058.

41 W. Meng, Y. Wen, L. Dai, Z. He and L. Wang, A novel electrochemical sensor for glucose detection based on Ag@ZIF-67 nanocomposite, *Sens. Actuators, B*, 2018, **260**, 852–860, DOI: 10.1016/j.snb.2018.01.109.

42 N. Karikalan, M. Velmurugan, S. M. Chen and C. Karuppiah, Modern approach to the synthesis of Ni $(OH)_2$ decorated sulfur doped carbon nanoparticles for the nonenzymatic glucose sensor, *ACS Appl. Mater. Interfaces*, 2016, **8**, 22545–22553, DOI: 10.1021/acsami.6b07260.

43 J. Landers, G. Y. Gor and A. V. Neimark, Density functional theory methods for characterization of porous materials, *Colloids Surf., A*, 2013, **437**, 3–32, DOI: 10.1016/j.colsurfa.2013.01.007.

44 J. Rouquerol, P. Llewellyn and F. J. S. S. S. C. Rouquerol, Is the BET equation applicable to microporous adsorbents?, *Stud. Surf. Sci. Catal.*, 2007, **160**, 49–56, DOI: 10.1016/S0167-2991(07)80008-5.

45 D. S. Kolchanov, V. Slabov, K. Keller, E. Sergeeva, M. V. Zhukov, A. S. Drozdov and A. V. Vinogradov, Sol–gel magnetite inks for inkjet printing, *J. Mater. Chem. C*, 2019, **7**, 6426–6432, DOI: 10.1039/C9TC00311H.

46 X. Kong, R. Bai, S. Wang, B. Wu, R. Zhang and H. Li, Recovery of phosphorus from aqueous solution by magnetic TiO_2*/Fe_3O_4 composites, *Chem. Phys. Lett.*, 2022, **787**, 139234, DOI: 10.1016/j.cplett.2021.139234.

47 X. Q. Chen, H. X. Zhang and W. H. Shen, Preparation, and characterization of the magnetic Fe_3O_4@TiO_2 nanocomposite with the in-situ synthesis coating method, *Mater. Chem. Phys.*, 2018, **216**, 496–501, DOI: 10.1016/j.matchemphys.2018.06.037.

48 D. M. Vidyadharan, B. N. Meethal, V. P. Jyothilakshmi and S. Swaminathan, Highly transparent titania in mixed organic solvent with controlled surface area and porosity, *Sol. Energy*, 2021, **213**, 43–52, DOI: 10.1016/j.solener.2020.11.002.

49 X. Wang, Z. Jia, F. Liu, H. Liang, X. You, K. Wang, X. Lou, W. Shuang, L. Xiao, B. Cai and L. Yang, The template-free synthesis of hierarchically porous anatase TiO_2 *via* acid-etching for enhancing the cycling stability and reversible capacity of lithium ion batteries, *RSC Adv.*, 2016, **6**, 48985–48994, DOI: 10.1039/c6ra03821b.

50 P. V. Bakre, P. S. Volvoikar, A. A. Vernekar and S. G. Tilve, Influence of acid chain length on the properties of TiO_2 prepared by sol-gel method and LC–MS studies of methylene blue photodegradation, *J. Colloid Interface Sci.*, 2016, **474**, 58–67, DOI: 10.1016/j.jcis.2016.04.011.

51 D. Zywitzki, H. Jing, H. Tüysüz and C. K. Chan, High surface area, amorphous titania with reactive Ti^{3+} through a photo-assisted synthesis method for photocatalytic H_2 generation, *J. Mater. Chem. A*, 2017, **5**, 10957–10967, DOI: 10.1039/C7TA01614J.

52 J. Zheng, Y. Wu, Q. Zhang, Y. Li, C. Wang and Y. Zhou, Direct liquid phase deposition fabrication of waxberry-like magnetic Fe_3O_4@TiO_2 core-shell microspheres, *Mater. Chem. Phys.*, 2016, **181**, 391–396, DOI: 10.1016/j.matchemphys.2016.06.074.

53 S. Khashan, S. Dagher, N. Tit, A. Alazzam and I. Obaidat, Novel method for synthesis of Fe_3O_4@TiO_2 core/shell nanoparticles, *Surf. Coat. Technol.*, 2017, **322**, 92–98, DOI: 10.1016/j.surfcoat.2017.05.045.

54 F. Parast, M. Montazeri-Pour, M. Rajabi and F. Bavarsiha, Comparison of the structural and photocatalytic properties of nanostructured Fe_3O_4/TiO_2 core–shell composites synthesized by ultrasonic and Stöber methods, *Sci. Sintering*, 2020, **52**, 415–432, DOI: 10.2298/SOS2004415P.

55 S. Samadi, A. Ashouri and M. Samadi, Synthesis of chiral allylic esters by using the new recyclable chiral heterogeneous oxazoline-based catalysts, *ACS Omega*, 2020, **5**, 22367–22378, DOI: 10.1021/acsomega.0c02764.

56 M. A. Tarighat, A. Rezaei and G. Abdi, Efficient catalytic extraction of metal ions in some Persian Gulf algae samples using Fe_3O_4@SiO_2-(3-chloropropyl) trimethoxysilane-L-cysteine nanocomposite and clustering of water samples according to alga metal pollution, *Appl. Nanosci.*, 2024, **14**, 89–107, DOI: 10.1007/s13204-023-02949-5.

57 J. N. Appaturi, M. R. Johan, R. J. Ramalingam and H. A. Al-Lohedan, Highly efficient green mesostructured urea functionalized on SBA-15 catalysts for selective synthesis of benzlidenemalononitrile, *Microporous Mesoporous Mater.*, 2018, **256**, 67–74, DOI: 10.1016/j.micromeso.2017.07.055.

58 K. Ö. Hamaloğlu, E. Sağ, Ç. Kip, E. Şenlik, B. S. Kaya and A. Tuncel, Magnetic-porous microspheres with synergistic catalytic activity of small-sized gold nanoparticles and titania matrix, *Front. Chem. Sci. Eng.*, 2019, **13**, 574–585, DOI: 10.1007/s11705-019-1799-y.

59 G. Mohammadnezhad, M. Esfandiari and F. Steiniger, End-grafted Cu-NNN pincer complexes on PAMAM dendrimers-SiO_2: synthesis and characterization, *New J. Chem.*, 2020, **44**, 15054–15065, DOI: 10.1039/d0nj02693j.

60 S. Majumder, S. Dey, K. Bagani, S. K. Dey, S. Banerjee and S. Kumar, A comparative study on the structural, optical and magnetic properties of Fe_3O_4 and Fe_3O_4@SiO_2 core–shell microspheres along with an assessment of their potentiality as electrochemical double layer capacitors, *Dalton Trans.*, 2015, **44**, 7190–7202, DOI: 10.1039/C4DT02551B.

61 F. Mushtaq, X. Chen, S. Staufert, H. Torlakcik, X. Wang, M. Hoop, A. Gerber, X. Li, J. Cai, B. J. Nelson and S. Pané, On-the-fly catalytic degradation of organic pollutants using magneto-photoresponsive bacteria-templated microcleaners, *J. Mater. Chem. A*, 2019, **7**, 24847–24856, DOI: 10.1039/C9TA06290D.

62 E. Norabadi, A. Jahantiq and H. Kamani, Synthesis of Fe-TiO_2@Fe_3O_4 magnetic nanoparticles as a recyclable sonocatalyst for the degradation of 2,4-dichlorophenol, *Environ. Sci. Pollut. Res.*, 2023, **30**, 31446–31460, DOI: 10.1007/s11356-022-24345-2.

63 M. M. Mohamed, W. A. Bayoumy, M. E. Goher, M. H. Abdo and T. M. El-Ashkar, Optimization of α-Fe_2O_3@Fe_3O_4 incorporated N-TiO_2 as super effective photocatalysts under visible light irradiation, *Appl. Surf. Sci.*, 2017, **412**, 668–682, DOI: 10.1016/j.apsusc.2017.03.200.

64 M. Stefan, O. Pana, C. Leostean, C. Bele, D. Silipas, M. Senila and E. Gautron, Synthesis and characterization of Fe_3O_4–TiO_2 core-shell nanoparticles, *J. Appl. Phys.*, 2014, **116**, 114312, DOI: 10.1063/1.4896070.

65 M. Qiao, X. Lei, Y. Ma, L. Tian, X. He, K. Su and Q. Zhang, Application of yolk–shell Fe_3O_4@N-doped carbon nanochains as highly effective microwave-absorption material, *Nano Res.*, 2018, **11**, 1500–1519, DOI: 10.1007/s12274-017-1767-0.

66 B. Dey, M. W. Ahmad, G. Sarkhel, D. J. Yang and A. Choudhury, Fabrication of porous nickel(II)-based MOF@carbon nanofiber hybrid mat for high-performance nonenzymatic glucose sensing, *Mater. Sci. Semicond. Process.*, 2022, **142**, 106500, DOI: 10.1016/j.mssp.2022.106500.

67 X. Wang, Z. Jia, F. Liu, H. Liang, X. You, K. Wang, X. Lou, W. Shuang, L. Xiao, B. Cai and L. Yang, The template-free synthesis of hierarchically porous anatase TiO_2 *via* acid-etching for enhancing the cycling stability and reversible capacity of lithium ion batteries, *RSC Adv.*, 2016, **6**, 48985–48994, DOI: 10.1039/C6RA03821B.

68 X. Q. Chen, H. X. Zhang and W. H. Shen, Preparation and characterization of the magnetic Fe_3O_4@TiO_2 nanocomposite with the in-situ synthesis coating method, *Mater. Chem. Phys.*, 2018, **216**, 496–501, DOI: 10.1016/j.matchemphys.2018.06.037.

69 M. P. Ravikumar, S. Bharathkumar, B. Urupalli, M. K. Murikinati, S. Muthukonda Venkatakrishnan and S. Mohan, Insights into the photocatalytic memory effect of magneto-plasmonic Ag–Fe_3O_4@TiO_2 ternary nanocomposites for dye degradation and H_2 production under light and dark conditions, *Energy Fuels*, 2022, **36**, 11503–11514, DOI: 10.1021/acs.energyfuels.2c01563.

70 M. Habibi Zare and A. Mehrabani-Zeinabad, Rational design and synthesis of 3D nanoreactors for green fuel production: design band gap Y@DS photocatalyst under visible irradiation, *ACS Appl. Energy Mater.*, 2023, **6**, 3173–3199, DOI: 10.1021/acsaem.2c02159.

71 S. Ishak, S. Mandal, H. S. Lee and J. K. Singh, Microencapsulation of stearic acid with SiO_2 shell as phase change material for potential energy storage, *Sci. Rep.*, 2020, **10**, 15023, DOI: 10.1038/s41598-020-71940-9.

72 G. G. Lara, G. F. Andrade, M. F. Cipreste, W. M. da Silva, P. L. Gastelois, D. A. Gomes, M. C. de Miranda, W. A. de Almeida Macedo, M. J. Neves and E. M. B. de Sousa, Protection of normal cells from irradiation bystander effects by silica-flufenamic acid nanoparticles, *J. Mater. Sci.: Mater. Med.*, 2018, **29**, 1–14, DOI: 10.1007/s10856-018-6134-5.

73 I. Dindarloo Inaloo, S. Majnooni, H. Eslahi and M. Esmaeilpour, Nickel(II) nanoparticles immobilized on EDTA-modified Fe_3O_4@SiO_2 nanospheres as efficient and recyclable catalysts for ligand-free Suzuki–Miyaura coupling of aryl carbamates and sulfamates, *ACS Omega*, 2020, **5**, 7406–7417, DOI: 10.1021/acsomega.9b04450.

74 H. J. Kim, J. Seo and M. J. Rose, H_2 photogeneration using a phosphonate-anchored Ni–PNP catalyst on a band-edge-modified p-Si (111)|AZO Construct, *ACS Appl. Mater. Interfaces*, 2016, **8**, 1061–1066, DOI: 10.1021/acsami.5b09902.

75 Z. Chen, R. Zheng, T. Bao, T. Ma, W. Wei, Y. Shen and B. J. Ni, Dual-doped nickel sulfide for electro-upgrading polyethylene terephthalate into valuable chemicals and hydrogen fuel, *Nanomicro Lett.*, 2023, **15**, 210, DOI: 10.1007/s40820-023-01181-8.

76 N. Zhao, X. Fei, X. Cheng and J. Yang, Synthesis of silver/silver chloride/graphene oxide composite and its surface-enhanced Raman scattering activity and self-cleaning property, *Mater. Sci. Eng.*, 2017, **242**, 012002, DOI: 10.1088/1757-899X/242/1/012002.

77 M. Thommes, K. Kaneko, A. V. Neimark, J. P. Olivier, F. Rodriguez-Reinoso, J. Rouquerol and K. S. Sing, Physisorption of gases, with special reference to the evaluation of surface area and pore size distribution (IUPAC Technical

Report), *Pure Appl. Chem.*, 2015, **87**, 1051–1069, DOI: 10.1515/pac-2014-1117.

78 P. Sharma, J. Prakash, T. Palai and R. Kaushal, Surface functionalization of bamboo leave mediated synthesized SiO_2 nanoparticles: Study of adsorption mechanism, isotherms and enhanced adsorption capacity for removal of Cr(VI) from aqueous solution, *Environ. Res.*, 2022, **214**, 113761, DOI: 10.1016/j.envres.2022.113761.

79 P. Maheswari, S. Harish, M. Navaneethan, C. Muthamizhchelvan, S. Ponnusamy and Y. Hayakawa, Biomodified TiO_2 nanoparticles with Withania somnifera, Eclipta prostrata and Glycyrrhiza glabra for anticancer and antibacterial applications, *Mater. Sci. Eng., C*, 2020, **108**, 110457, DOI: 10.1016/j.msec.2019.110457.

80 D. Anbumani, K. vizhi Dhandapani, J. Manoharan, R. Babujanarthanam, A. K. H. Bashir, K. Muthusamy, A. Alfarhan and K. Kanimozhi, Green synthesis and antimicrobial efficacy of titanium dioxide nanoparticles using Luffa acutangula leaf extract, *J. King Saud Univ., Sci.*, 2022, **34**, 101896, DOI: 10.1016/j.jksus.2022.101896.

81 N. El-Shafai, M. E. El-Khouly, M. El-Kemary, M. Ramadan, I. Eldesoukey and M. Masoud, Graphene oxide decorated with zinc oxide nanoflower, silver and titanium dioxide nanoparticles: fabrication, characterization, DNA interaction, and antibacterial activity, *RSC Adv.*, 2019, **9**, 3704–3714, DOI: 10.1039/C8RA09788G.

82 F. Wang, X. Chen, L. Chen, J. Yang and Q. Wang, High-performance nonenzymatic glucose sensor by hierarchical flower-like nickel(II)-based MOF/carbon nanotubes composite, *Mater. Sci. Eng., C*, 2019, **96**, 41–50, DOI: 10.1016/j.msec.2018.11.004.

83 Y. Chen, B. Liu, Z. Chen and X. Zuo, Innovative electrochemical sensor using TiO_2 nanomaterials to detect phosphopeptides, *Anal. Chem.*, 2021, **93**, 10635–10643, DOI: 10.1021/acs.analchem.1c01973.

84 H. Yin, X. Bai and Z. Yang, Activating Ni nanoparticles into Ni single atoms by N doping for high-performance electrochemical sensing of glucose, *Chem. Eng. J.*, 2023, **478**, 147510, DOI: 10.1016/j.cej.2023.147510.

85 T. Xu, Y. Zhang, M. Liu, H. Wang, J. Ren, Y. Tian, X. Liu, Y. Zhou, J. Wang, W. Zhu and M. Ma, In-situ two-step electrodeposition of α-CD-rGO/Ni-MOF composite film for superior glucose sensing, *J. Alloys Compd.*, 2022, **923**, 166418, DOI: 10.1016/j.jallcom.2022.166418.

86 A. Walcarius, Mesoporous materials and electrochemistry, *Chem. Soc. Rev.*, 2013, **42**, 4098–4140, DOI: 10.1039/C2CS35322A.

87 A. A. Ensafi, N. Ahmadi and B. Rezaei, Nickel nanoparticles supported on porous silicon flour, application as a nonenzymatic electrochemical glucose sensor, *Sens. Actuators, B*, 2017, **239**, 807–815, DOI: 10.1016/j.snb.2016.08.088.

88 Y. Zhang, Y. Wang, J. Jia and J. Wang, Nonenzymatic glucose sensor based on graphene oxide and electrospun NiO nanofibers, *Sens. Actuators, B*, 2012, **171**, 580–587, DOI: 10.1016/j.snb.2012.05.037.

89 N. S. Lopa, M. M. Rahman, F. Ahmed, S. C. Sutradhar, T. Ryu and W. Kim, A Ni-based redox-active metal–organic framework for sensitive and nonenzymatic detection of glucose, *J. Electroanal. Chem.*, 2018, **822**, 43–49, DOI: 10.1016/j.jelechem.2018.05.014.

90 M. Waqas, L. Yang, Y. Wei, Y. Sun, F. Yang, Y. Fan and W. Chen, Controlled fabrication of nickel and cerium mixed nano-oxides supported on carbon nanotubes for glucose monitoring, *Electrochim. Acta*, 2023, **440**, 141735, DOI: 10.1016/j.electacta.2022.141735.

91 R. A. Soomro, Z. H. Ibupoto, M. I. Abro and M. Willander, Electrochemical sensing of glucose based on novel hedgehog-like NiO nanostructures, *Sens. Actuators, B*, 2015, **209**, 966–974, DOI: 10.1016/j.snb.2014.12.050.

92 M. Li, X. Bo, Z. Mu, Y. Zhang and L. Guo, Electrodeposition of nickel oxide and platinum nanoparticles on electrochemically reduced graphene oxide film as a nonenzymatic glucose sensor, *Sens. Actuators, B*, 2014, **192**, 261–268, DOI: 10.1016/j.snb.2013.10.140.

93 X. Zhang, Z. Zhang, Q. Liao, S. Liu, Z. Kang and Y. Zhang, Nonenzymatic glucose sensor based on in situ reduction of Ni/NiO-graphene nanocomposite, *Sensors*, 2016, **16**, 1791, DOI: 10.3390/s16111791.

94 B. Dey, M. W. Ahmad, G. Sarkhel, D. J. Yang and A. Choudhury, Fabrication of porous nickel(II)-based MOF@carbon nanofiber hybrid mat for high-performance nonenzymatic glucose sensing, *Mater. Sci. Semicond. Process.*, 2022, **142**, 106500, DOI: 10.1016/j.mssp.2022.106500.

95 P. Yang, X. Tong, G. Wang, Z. Gao, X. Guo and Y. Qin, NiO/SiC nanocomposite prepared by atomic layer deposition used as a novel electrocatalyst for nonenzymatic glucose sensing, *ACS Appl. Mater. Interfaces*, 2015, **7**, 4772–4777, DOI: 10.1021/am508508m.